A&A 497, 291–310 (2009)
DOI: 10.1051/0004-6361/20077892

Astronomy & Astrophysics

Effective area calibration of the reflection grating spectrometers of XMM-Newton

I. X-ray spectroscopy of the Crab nebula

J. S. Kaastra[1,2], C. P. de Vries[1], E. Costantini[1,2], and J. W. A. den Herder[1]

[1] SRON Netherlands Institute for Space Research, Sorbonnelaan 2, 3584 CA Utrecht, The Netherlands
e-mail: J.S.Kaastra@sron.nl
[2] Sterrenkundig Instituut, Universiteit Utrecht, PO Box 80000, 3508 TA Utrecht, The Netherlands

Received 15 May 2007 / Accepted 15 January 2009

ABSTRACT

Context. The Crab nebula and pulsar have been widely used as a calibration source for X-ray instruments. The in-flight effective area calibration of the Reflection Grating Spectrometers (RGS) of XMM-Newton depend upon the availability of reliable calibration sources.
Aims. We investigate how the absolute effective area calibration of RGS can be obtained using Crab as a standard candle.
Methods. We have analysed RGS observations of the Crab using different instrument configurations and spatial offsets, and made use of previous determinations of the continuum spectrum of the nebula plus pulsar. Due to the high spectral resolution of the RGS, we resolve the main absorption edges and detect the strong 1s−2p absorption lines of neutral oxygen.
Results. We get an excellent fit to the Crab spectrum using this fixed continuum and the absorption spectrum determined by RGS. We get accurate column densities for the neutral atoms of H, N, O, Ne, Mg, and Fe, as well as a clear detection of Fe II and firm upper limits for other ions. Our data are in good agreement with earlier optical and UV spectroscopic measurements of some of these ions. We find solar abundances for N and O, while Ne is overabundant by a factor of 1.7 and Fe is underabundant by a factor of 0.8. We confirm that there is less dust in the line of sight compared to the prediction based on the absorption column. Our spectra suggest a more prominent role of ferric iron in the dust compared to ferrous iron.
Conclusions. Our high-resolution observations confirm that Crab can be used as an X-ray calibration source. RGS spectra have determined the absorption spectrum towards Crab with unprecedented detail.

Key words. instrumentation: spectrographs – ISM: abundances – dust, extinction – ISM: supernova remnants – X-rays: ISM – X-rays: individuals: Crab

1. Introduction

The Crab nebula and pulsar have been widely used as a calibration source for X-ray instruments, starting already in the early days of X-ray astronomy. The main advantage of Crab is that it is one of the brightest steady X-ray sources on the sky and that it has a simple power-law spectrum.

Later, more complexities of the spectrum have become clear. For instance, recent imaging data (XMM-Newton: Willingale et al. 2001; Chandra: Weisskopf et al. 2000; Mori et al. 2004) show a complex spectral and spatial structure with the components such as pulsar, torus, jet, dust-scattering halo, etc. Also, the spectral shape of the pulsar and nebula are different, and both show spectral breaks at higher energies (e.g., Kuiper et al. 2001).

A complicating factor is that the interstellar absorption becomes very high at low energies. For many instruments, the uncertainties in the low-energy calibration of the instruments is formally compensated for by adjusting the interstellar absorption column density to get a best fit. This procedure, however, introduces high systematic errors both in the derived effective area at low energies, as well as in the derived interstellar absorption. This issue is illustrated by Kirsch et al. (2005), who compare a large number of current and past X-ray instruments that have observed Crab.

There is still an urgent need for accurate calibration of X-ray instruments in space. First, an accurate knowledge of the relative effective area is needed for sources with complex intrinsic continua, for example active galactic nuclei with warm absorbers, relativistically broadened iron or oxygen lines, soft spectral components and hard reflection components. Furthermore, an accurate knowledge of the absolute effective area is important when X-ray data are to be matched to optical/UV data (for example for isolated neutron stars), or where the absolute flux has cosmological implications. A good example of the last issue are clusters of galaxies; their absolute flux determines their absolute hot gas mass as well as the inferred baryonic fraction.

The problem with most previous and current X-ray instruments that have observed Crab is their relatively poor spectral resolution at the low energies where interstellar absorption is important. The situation has improved considerably by the advent of high-resolution grating spectrometers. With high spectral resolution, it is possible to resolve the absorption edges and absorption lines, thereby constraining the interstellar absorption. With the Chandra Low Energy Transmission Grating

Spectrometer (LETGS) it has been possible to obtain a high resolution spectrum of the Crab pulsar (Tennant et al. 2001), but the nebula containing most of the X-ray flux is too extended for the LETGS to obtain a high resolution spectrum. On the other hand, the Reflection Grating Spectrometers (RGS) of XMM-Newton (den Herder et al. 2001) are well-suited to observe the full Crab nebula.

From an astrophysical point of view, these Crab spectra offer us a unique opportunity to study the interstellar medium. For instance, the determination of the interstellar abundances from optical and UV spectroscopy is not straightforward, as only the gaseous components yield absorption lines. Moreover, these absorption lines are often heavily saturated, thereby making an accurate determination of ionic column densities difficult. Furthermore, depletion of free atoms onto dust complicates the situation considerably. In X-ray spectra essentially all atoms, whether in gaseous or molecular form, contribute to the X-ray opacity, and the correction factors for differences in dust and gaseous opacity are not very high. Moreover, high-resolution spectra near the dominant absorption edges can help to disentangle the gaseous from the dusty or molecular phases, and to give clues on the chemical composition of the dust.

In this paper we analyse a set of observations of the Crab nebula, obtained with the RGS of XMM-Newton. These data were taken for the purpose of effective area calibration. The paper is laid out as follows. In Sect. 2 we discuss the intrinsic (unabsorbed) continuum spectrum of Crab as derived from other instruments. In Sect. 3 we describe the basic data extraction and non-standard instrumental corrections that we need to apply. Section 3 then presents the results of our spectral analysis. In Sect. 4 we discuss our results on the interstellar absorption and the composition of the interstellar medium towards Crab. In Sect. 5 we discuss the implications for the calibration of the RGS and give a breakdown of the systematic uncertainties involved in this calibration. Our conclusions are given in Sect. 6.

This paper is the first of a series of three papers. In Paper II (Kaastra et al. 2009b) we present a new analysis of the X-ray model spectra of the white dwarfs Sirius B and HZ 43. We show in that paper how these models can be used to calibrate the long wavelength absolute effective area of the LETGS of Chandra with an accuracy of a few percent. In Paper III (Kaastra et al. 2009a) we combine these results based on white dwarfs with our present results on Crab using blazar spectra taken simultaneously with the RGS and LETGS. This leads to a refinement of the calibration presented in the present paper, and allows to determine the absolute flux of Crab within a few percent uncertainty.

2. The intrinsic spectrum of the Crab nebula and pulsar

2.1. The Crab nebula as a calibration source

Toor & Seward (1974) have studied the Crab nebula as a potential calibration source for X-ray astronomy. They measured Crab in 1970 using a rocket experiment with proportional counters between 1.5−10 keV and scintillation counters between 5−70 keV. The measured spectrum (nebula + pulsar) has a power-law with photon index $\Gamma = 2.10 \pm 0.03$ and normalisation N at 1 keV of 9.7 ± 1.0 (in units of 10^4 photons m^{-2} s^{-1} keV^{-1}, used throughout this paper for the Crab normalisation). Apparently no correction for Galactic absorption at the lowest energies was made.

If we fit the data as presented by Toor & Seward, we find instead $\Gamma = 2.13 \pm 0.05$ and $N = 10.3 \pm 0.9$, i.e. a slightly steeper power-law. Correcting their data for Galactic absorption using simply Morrison & McCammon (1983) absorption cross sections and $N_{\rm H} = 3.45 \times 10^{25}$ m^{-2} (Schattenburg & Canizares 1986), we obtain a 20% higher flux at 1.7 keV, the lowest energy measured by Toor & Seward. This results in $\Gamma = 2.18 \pm 0.05$ and $N = 11.5 \pm 1.0$, i.e. an increase in Γ of 0.05.

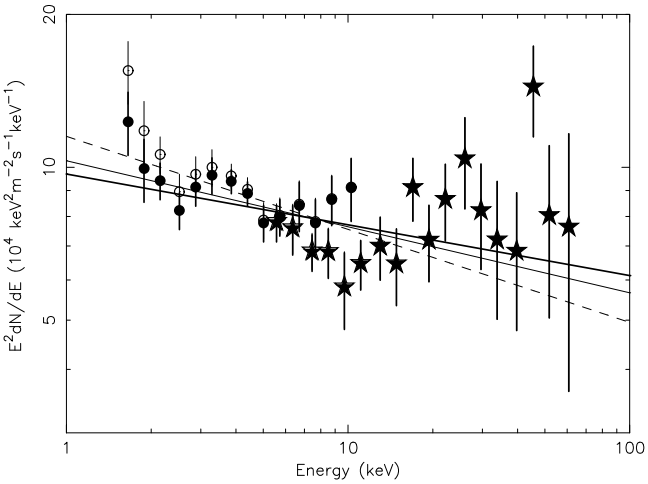

Fig. 1. Measurements of the Crab nebula by Toor & Seward (1974). Circles: proportional counter; stars: scintillation counter; filled symbols: data from Fig. 3 of Toor & Seward; open symbols: same data but corrected for Galactic absorption. Thick solid line: power-law model of Toor & Seward; thin solid line: our power-law fit to the same data; dashed line: power-law fit to absorption corrected data.

Figure 1 shows a comparison between these fits and the raw and absorption-corrected data of Toor & Seward. It is evident that at any energy the uncertainty in the spectrum is at least 10%. Also note the discrepancy between both instruments near 10 keV: the scintillation counter measures about 13% less flux in the common 5−11 keV band.

From the above discussion it is clear that we need to pay more attention to the way the spectral parameters of Crab are derived and to their statistical and systematic uncertainties. As it is known that the pulsar and the nebula have a different spectrum, we also have to derive both model spectra separately, even though our RGS observations have insufficient spatial and time resolution to distinguish both.

Since the early work of Toor & Seward (1974), many measurements of the Crab spectrum using different instruments have been made, see for instance Kirsch et al. (2005) for an overview. Not all of these measurements are suitable for our purpose. Most instruments operating only in the energy band below 10 keV have hard times in determining reliable spectral indices. This is because at low energies the effects of 1) low spectral resolution; 2) complicated instrumental effective area structures like filter edges etc.; 3) a complex redistribution function and 4) the strong impact of interstellar absorption all conspire to make an accurate flux measurement at low energies and thereby a reliable photon index in the 1−10 keV band a hard to determine quantity. At higher energies all these effects are less important. For this reason, the data set that we use for the spectral parameters of Crab is taken from the analysis of BeppoSAX and other data as presented by Kuiper et al. (2001). These are based on a careful analysis of the spectrum in a very broad band, separating the pulsar and nebula component, and although there still is a 10% uncertainty in the absolute flux scale of those data, the spectral shape is very well determined, as elaborated below.

2.2. The X-ray spectrum of the Crab pulsar

Kuiper et al. (2001, K01 hereafter) have studied Crab extensively using data from BeppoSAX, Comptel and EGRET. From their paper, we find the best spectrum of the pulsar to be given by

$$F_{\rm p} = 726E^{-1.276}{\rm e}^{-0.074x^2} + 1464E^{-1.165}{\rm e}^{-0.159x^2} + 2021E^{-2.022}, \quad (1)$$

where E is the photon energy in keV, $x \equiv \ln E$ and $F_{\rm p}(E)$ the spectrum in photons m^{-2} s^{-1} keV^{-1}. This spectrum needs to be corrected for absorption by the intervening ISM, for which K01 used Morrison & McCammon (1983) cross sections with $N_{\rm H} = 3.61 \times 10^{25}$ m^{-2}.

2.3. The neutron star (unpulsed) emission

The spectrum of the pulsar as described by K01 only contains the pulsed emission. There is also steady emission. Tennant et al. (2001) estimate the zeroth order count rate of the steady neutron star emission as measured by the Chandra LETGS as 0.19 counts s^{-1}. For comparison, the total (dead-time corrected) zeroth order count rate is 8.16 counts s^{-1}, hence the steady emission is only 2.3% of the total emission. Weisskopf et al. (2004) estimated the steady neutron star emission from the LETGS spectrum. For a distance of 2 kpc and a radius of 15.6 km, they find a 2σ upper limit to the temperature of 0.159 keV. Such a spectrum produces only 0.3−1% of the total point source emission over the full LETGS range, 1% being reached around 0.8 keV. Hence we conclude that the contribution of the unpulsed emission can be neglected for the present purpose.

2.4. The X-ray spectrum of the Crab nebula

A simple power-law approximation for the nebula or the pulsar over the full X-ray and γ-ray energy range is inadequate. At higher energies, the spectrum of Crab softens. This was shown by K01 using Comptel data and by Ling & Wheaton (2003) using BATSE data. The break of about 0.3 in photon index occurs around 100 keV. Ling & Wheaton give an average photon index of 2.1 ± 0.1 below the break at 120 ± 40 keV and $\Gamma = 2.4 \pm 0.2$ above the break. Therefore, we will limit the range of validity of any power-law approximation to $E < 100$ keV.

K01 also studied the spectrum of the nebula only (pulsar subtracted). These data are available at `http://www.sron.nl/divisions/hea/kuiper/data.html`. From their data, we find the best fit power-law based upon BeppoSAX MECS data only to be $\Gamma = 2.146 \pm 0.003$ and $N = 9.31 \pm 0.05$ (no systematic uncertainty included). We have fitted all BeppoSAX data as given by K01 (MECS, HPGSPC and PDS, excluding LECS) in the 1−100 keV band using a simple power-law, and scaling the model for HPGSPC by a factor of 1.01 and PDS by a factor of 0.87 with respect to MECS, following K01. We excluded LECS because it is more sensitive to Galactic absorption and also because its spatial and spectral resolution decreases rapidly for lower energies, making it more prone to possible systematic uncertainties. The best fit power-law has $\Gamma = 2.147 \pm 0.002$ and $N = 9.31 \pm 0.05$, in excellent agreement with the fit to MECS only. We show the fit in Fig. 2. Because the residuals are dominated by small remaining systematic variations of less than 1, 2 and 4% for MECS, HPGSPC and PDS, respectively, we have used an unweighted fit through these data points. Hence our adopted model for the nebula is given by

$$F_{\rm n} = 9.31 \times 10^4 E^{-2.147} \quad (2)$$

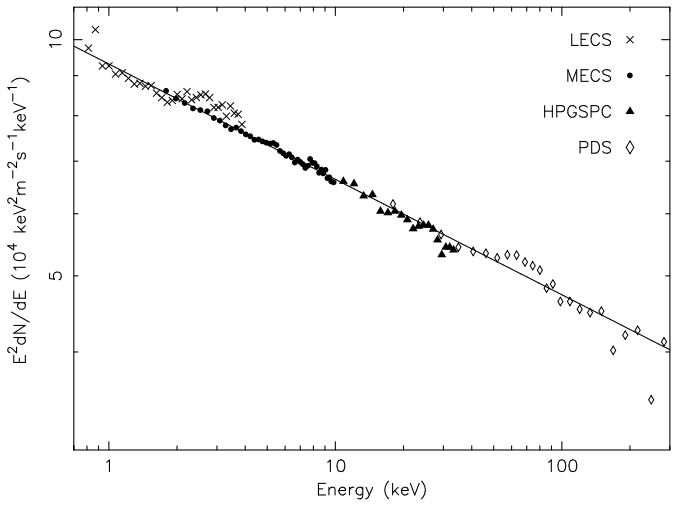

Fig. 2. BeppoSAX measurements of the Crab nebula from Kuiper et al. (2001). The pulsar has been subtracted and the fluxes have been corrected for Galactic absorption as described in the text. LECS, HPGSPC and PDS data have been divided by 0.93, 1.01 and 0.87, respectively. For clarity, error bars (all lower than the plot symbols) have been omitted. The solid line indicates the best fit power-law excluding LECS) with $\Gamma = 2.147 \pm 0.002$ and $N = 9.31 \pm 0.05$.

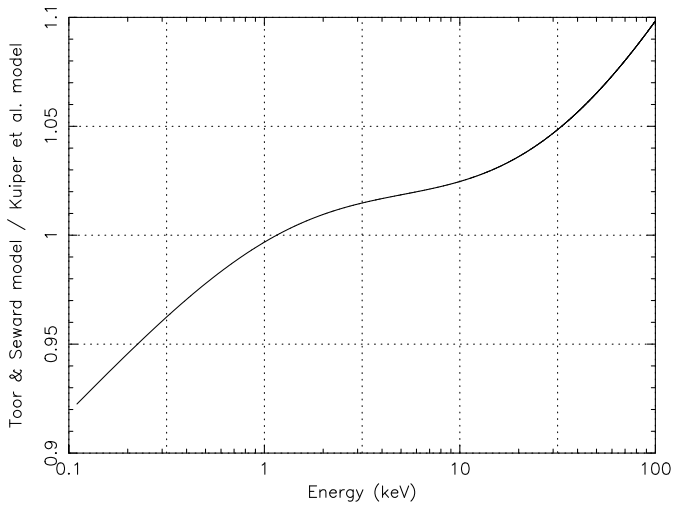

Fig. 3. Comparison between the model spectra for the full Crab nebula and pulsar. Shown is the ratio between the power-law model of Toor & Seward (1974) and the more complicated model of Kuiper et al. (2001).

where again E is the photon energy in keV and $F_{\rm n}(E)$ the nebular spectrum in photons m^{-2} s^{-1} keV^{-1}.

In Fig. 3 we compare the model spectra of Toor & Seward with the combined nebula + pulsar spectrum of K01. It is seen that in the MECS band (1−10 keV) both models agree within 2%; the differences are higher near 100 keV (up to 10%) and at low energies (8% at 0.1 keV).

2.5. Intrinsic curvature of the Crab nebula spectrum

The K01 power-law model for the nebula that we use here is reasonably well established for energies above 2 keV. However, below 2 keV interstellar absorption becomes important. The usual approach with low-resolution instruments has been to assume that the power-law extends unbroken down to about 0.5 keV, and to adjust the interstellar column density until a good spectral fit at low energies is obtained. This approach was also used by K01.

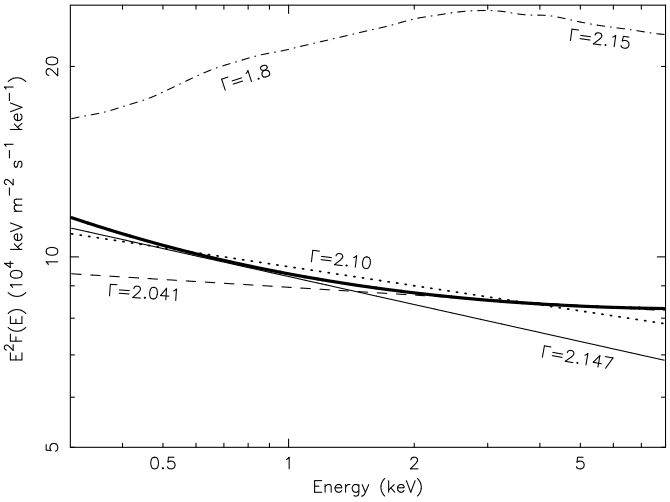

Fig. 4. Unabsorbed continuum spectrum of the Crab nebula. Thin solid line ($\Gamma = 2.147$): power-law model of Kuiper et al. (2001). Thick solid line: integrated spectrum derived from the Chandra maps of photon index and count rate as given by Mori et al. (2004). Dashed line ($\Gamma = 2.041$): power-law approximation to the above integrated Chandra spectrum in the 2−8 keV band. Dotted line ($\Gamma = 2.10$): direct power-law fit of Mori et al. (2004) to the full nebula spectrum. Dash-dotted line: theoretical model spectrum (run A) determined by Del Zanna et al. (2006).

There is no guarantee, however, that the power-law is unbroken below 2 keV. The evidence that the spectrum is not a simple power-law comes from both theoretical considerations and observations.

2.5.1. Theoretical considerations

The Crab nebula emits synchrotron emission due to the motion of accelerated particles in a magnetic field. By its nature, such radiation has a high-energy cut-off corresponding to the maximum energy of the particles. Del Zanna et al. (2006) have made detailed magneto-hydrodynamical models for pulsar nebulae with synchrotron emission incorporated self-consistently. Their model A was chosen to have parameters relevant for the Crab nebula. That model describes the spectral morphology of the nebula qualitatively well. The integrated spectrum shows multiple breaks due to spatially varying maximum particle energies. In the X-ray band, their integrated model spectrum has a break around 3 keV, with a slope of 1.8 below it and 2.15 above it (dash-dotted line in Fig. 4). However, this model over-predicts the observed X-ray flux at 1 keV by a factor of 2, and another model B – although less consistent with the morphology of the Crab nebula – has spectral breaks at different energies. What we gather from these models is therefore that spectral breaks in the integrated X-ray spectrum may occur between 0.5 and 10 keV, but the details of where they occur and how strong they are are hard to predict exactly.

2.5.2. Observational evidence of spectral curvature

Evidence of spectral breaks also comes from spectral imaging studies of the Crab nebula. There are clear spatial variations of the photon index over the surface of the nebula, as for example observed with XMM-Newton (Willingale et al. 2001). Using Chandra ACIS-S data, Mori et al. (2004, M04 hereafter) fitted simple power-laws to the local spectrum of small regions and produced a map of the total count rate and photon index Γ. They fixed the Galactic absorption to $N_{\rm H} = 3.2 \times 10^{25}$ m^{-2}. The photon index ranges between 1.5 and 3.1, implying that the integrated spectrum must show curvature. We have converted the 0.5−8 keV count rate map of M04 into flux using version 3.7 of PIMMS for calculating the photon-index dependent conversion curve. The total nebular spectrum was calculated by adding the individual spectra of the small regions. This total spectrum indeed shows curvature (thick solid line in Fig. 4), although over the 0.3−8 keV band it never deviates more than 5% from the simple power-law with $\Gamma = 2.10$ as determined directly from a spectral fit to the integrated spectrum (M04).

Our aim is to determine how much the low-energy continuum is enhanced relative to the high-energy power-law spectrum. We saw that the 1−100 keV integrated nebula spectrum as determined by other instruments shows no breaks (K01; Sect. 2.4). K01 put some question marks to the robustness of their fit below 1 keV, because of the complexity of the spectral/spatial redistribution function of the BeppoSAX LECS in that band. Moreover, below 2 keV the interstellar absorption affects the spectrum more than 2% (below 1 keV more than 8%) introducing additional uncertainties. Therefore we determine the spectral curvature relative to the well-determined 2−8 keV continuum.

The spatially integrated curved spectrum in the 2−8 keV band is approximated by a single power-law with $\Gamma = 2.041$, to within 1% accuracy (see Fig. 4). We define the intrinsic curvature correction function $f_{\rm c}(E)$ as the ratio of the full integrated spectrum to this 2−8 keV power-law approximation. The correction factor $f_{\rm c}(E)$ is shown in Fig. 5. At $E = 0.5$ keV, the integrated spectrum is 13% higher than the power-law approximation, showing the importance of the correction. We will use a simple analytical approximation for $f_{\rm c}(E)$:

$$f_{\rm c}(E) = 1 + 0.411{\rm e}^{-{\rm E}/0.46} \qquad (3)$$

where E is the photon energy in keV. The accuracy of this approximation is better than 1%, and over the RGS band (5−38 Å) it is even better than 0.6%.

The curvature correction derived above (3) represents the steepening of the soft X-rays with respect to the hard X-ray power-law spectrum, for the full Crab spectrum. The photon index of the nebula at high energies (2−8 keV) based on the Chandra data (2.041) differs by 0.106 from the photon index that we obtained in Sect. 2.4 based on K01 (2.147, see also Fig. 4). This difference may look surprisingly high, but can be explained well. The Chandra data were fitted in a low energy band (below 8 keV), where Galactic absorption cannot be neglected; moreover, the Galactic column density obtained by M04 is 4.1×10^{24} m^{-2} lower than the value used by K01. This leads to different ISM transmission factors that can be approximated to lowest order by a power-law over the 0.3−8 keV band with a slope of 0.087. Thus if M04 would have used a higher Galactic column density (like the K01 value), their photon indices would have been higher by 0.087, close to and within the systematic uncertainties of the K01 value. The question then arises why M04 arrived at a lower column density. This may be due to the spectral softening of the intrinsic nebula continuum associated with the curvature correction; furthermore, M04 derived their column density from the fainter regions of Crab, which are generally in the outer parts with intrinsically steeper spectra.

As the curvature correction gives the *relative change* in spectral index between the soft and hard band, and is based on the spatial variations of the local photon index, an overall change of

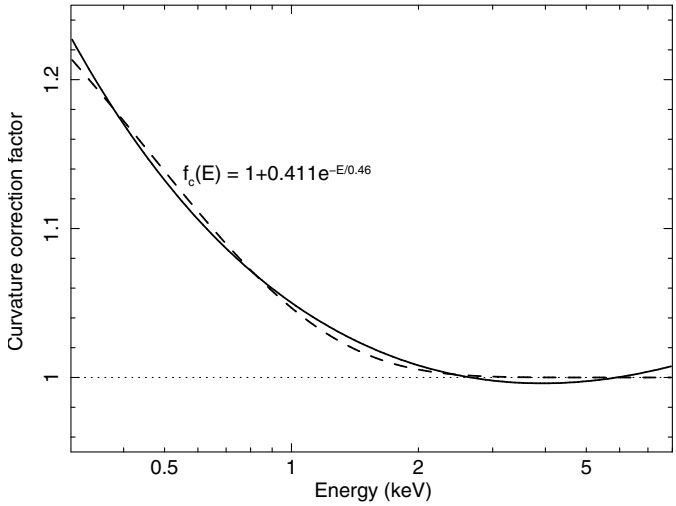

Fig. 5. Solid line: correction factor $f_c(E)$ for the intrinsic curvature of the continuum spectrum of the Crab nebula, obtained by comparing the full integrated model spectrum to a power-law approximation in the 2−8 keV band. Dashed line: analytical approximation to $f_c(E)$ (Eq. (3)).

all local photon indices due to accounting for systematic uncertainties does, to first order, only affect the integrated hard and soft band spectral slopes, but not their difference. In a similar way, a different treatment of the interstellar absorption will affect all spectral slopes in the same way and will not affect the curvature correction. Therefore, we apply the curvature correction (3) also to the K01 continuum.

As an independent test, we have used a MOS data set to derive the curvature correction in a similar way as described above for Chandra (we use the MOS observation of Appendix A.7). Within the statistical errors, we obtain the same curvature correction. See Appendix B.2 for more details and estimates of the uncertainties on the curvature correction.

The total, unabsorbed continuum spectrum of Crab (nebula plus pulsar) is then given by

$$F_p(E) + F_n(E) f_c(E), \tag{4}$$

where $F_p(E)$, $F_n(E)$ and $f_c(E)$ are given by (1)−(3), respectively. The systematic uncertainty on the slope of Crab at high energies ($F_p(E) + F_n(E)$) is estimated in Sect. B.1 to be 0.016. The systematic uncertainties on the curvature correction $f_c(E)$ are estimated in Sect. B.2, and give rise to systematic slope uncertainties lower than 0.010 over the RGS band.

In order to show the effects of this curvature correction, in our analysis of the RGS spectrum we also show fit results for the case of the K01 unbroken power-law without the curvature correction given by (3).

3. Observations and data analysis

3.1. Data selection

The data were taken on February 24 and 25, 2006, during orbit 1138 of XMM-Newton. We only discuss here the RGS observations. For each observation, either 1, 2, 4 or 8 CCDs were read out in a fixed sequence. This setup was done in order to study the effects of pile-up on the spectrum (see Appendix A.4). In addition, a set of observations with off-axis pointing in the cross-dispersion direction was done, with off-axis angles of ±3.5 and ±7.0 arcmin, in order to study the spatial distribution of the emission in the cross-dispersion direction (see Appendix A.6). A summary of the observations is shown in Table 1. The observations were processed using SAS version 7.0 and the set of calibration files (CCF) available October 2006. More information on the spectral extraction and the various correction factors that we need are given in Appendix A.

Table 1. Observation log.

ID[a]	seq. nr	RGS 1 or 2	CCDs in use	t_{exp} (ks)	$\Delta\theta^b$ (arcmin)
101	002	1	1	15.5	–
101	003	1	2	15.2	–
101	004	1	3	7.0	–
101	005	1	4	3.7	–
101	006	1	5	1.6	–
101	007	1	6	0.6	–
101	008	1	8	0.5	–
101	009	1	9	1.5	–
101	033	2	1	15.5	–
101	034	2	2	15.2	–
101	035	2	3	7.0	–
101	036	2	5	3.7	–
101	037	2	6	1.6	–
101	038	2	7	0.6	–
101	039	2	8	0.5	–
101	040	2	9	1.5	–
101	010	1	1,5	4.0	–
101	011	1	2,6	4.5	–
101	012	1	3,8	4.0	–
101	013	1	4,9	4.5	–
101	041	2	1,6	4.0	–
101	042	2	2,7	4.5	–
101	043	2	3,8	4.0	–
101	044	2	5,9	4.5	–
101	014	1	1,3,5,9	3.9	–
101	015	1	2,4,6,8	2.5	–
101	045	2	1,3,5,7	2.5	–
101	046	2	2,6,8,9	2.9	–
101	016	1	all	1.7	–
101	047	2	all	1.9	–
201	004	1	all	5.8	+3.5
201	005	2	all	5.8	+3.5
301	004	1	all	5.7	−3.5
301	005	2	all	5.7	−3.5
401	004	1	all	8.5	+7.0
401	005	2	all	8.5	+7.0
501	004	1	all	14.9	−7.0
501	005	2	all	14.9	−7.0

[a] Observation ID (the leading digits 0312790 are the same for all observations and have been omitted here); [b] off-axis angle in the cross-dispersion direction.

3.2. Spectral fitting

All spectral fitting was done using the SPEX package (Kaastra et al. 1996, see also `www.sron.nl/spex`). RGS1 and RGS2 data were fit simultaneously. The continuum model for Crab was taken to be the K01 model (pulsar plus nebula) discussed in Sects. 2.2 and 2.4, including the curvature correction derived in Sect. 2.5.2. This continuum model was read as a table (model *file* in SPEX), and the normalisation of this continuum was frozen. We apply two multiplicative components to this continuum, discussed below: a correction for the unknown effective area of the RGS, and a model for the interstellar absorption. Therefore in

our fit, the only free parameters are the properties of the interstellar absorption (column densities and line width), and the two parameters of the effective area correction.

As we indicated in Appendix A.2, the effective area of RGS has been determined modulo a power-law correction. The true effective area $A_{\rm true}(\lambda)$ as a function of the wavelength λ (in Å) can be related to the effective area currently present in the response matrix $A_{\rm resp}(\lambda)$ by $A_{\rm true}(\lambda) = f(\lambda)A_{\rm resp}(\lambda)$ where

$$f(\lambda) = A(\lambda/10)^{\alpha}. \quad (5)$$

For technical reasons we have chosen not to fit directly the parameters A and α, but to fit use $f(\lambda_1)$ and $f(\lambda_2)$ with $\lambda_{1,2}$ extreme points for the RGS band, chosen here as 5 and 40 Å.

For our absorption model, we use a combination of the *hot* and *slab* models of SPEX. Both models use the same set of atomic absorption cross sections (see below). The *slab* model calculates the transmission of a layer of plasma with arbitrary composition. Free parameters are the column densities of individual ions as well as the intrinsic velocity broadening. We use this model component for all neutral atoms of the elements that show clearly detectable absorption edges in the RGS band (N, O, Ne, Mg and Fe), plus their singly ionised ions (for detections or upper limits to the ionised fraction).

For all other elements we use the *hot* model. This model calculates the transmission of a plasma in collisional ionisation equilibrium. We use this with a very low temperature (the neutral gas limit). For the abundances of those elements we adopt the proto-solar abundances of Lodders (2003). The dominant contributors in the RGS band for those elements are He, H, C, Si and S (in order of importance). The cross sections of all these elements are tied to the hydrogen cross section.

The cross sections used for both the *hot* and *slab* models are described in more detail in the SPEX manual. Basically, both continuum and line opacity are taken into account. For neutral atoms in the RGS band predominantly inner shell absorption lines are important; the cross sections of those line were mainly calculated by Behar using the HULLAC code; see also Sect. 5.1 of Kaastra et al. (2002) for more details.

Alternatively, in order to investigate the role of dust, we have also made spectral fits with the model outlined above (which we label model A), but with a part of the total column replaced by a gas and dust mixture (model B). This gas and dust mixture is assumed to have also the proto-solar abundances of Lodders (2003), but a fraction of the gas is depleted into dust grains. The depletion factors of the dust are taken from Wilms et al. (2000). The transmission of the dust is calculated using the *dabs* model that we introduce here in the SPEX package, which follows completely the dust treatment as described by Wilms et al. (2000) and references therein. Basically, the grains are assumed to be spherical, fluffy ($\rho = 1000$ kg m^{-3}), and have a size distribution $dn/da \sim a^{-p}$ for the grain radius a between $a_{\rm min} < a < a_{\rm max}$, with default values $a_{\rm min} = 0.025\,\mu$m, $a_{\rm max} = 0.25\,\mu$m, and $p = 3.5$.

As a third model (Model C) we also made a fit without the curvature correction but further identical to model A, in order to investigate the effects of this curvature correction.

For the spectral fitting, we rebinned all data by a factor of 5 to account for the reduced spectral resolution caused by the spatial extent of Crab (0.22 Å *FWHM*, see Appendix A.7). This gives bins with a width of ~0.04 Å at 7 Å to 0.07 Å at 30 Å. Fitting was restricted in most cases to the 7–30 Å band; below 7 Å, scattering by the RGS gratings becomes very important, but theory of scattering at these short wavelengths starts to break down. Therefore, there is essentially no knowledge of the RGS effective area below 7 Å. Hence this wavelength range was excluded from the fit. Above 30 Å, the low energy of the X-ray events deposited on the CCD, combined with the extent of the source, starts to coincide with the tail of the CCD system peak. For this reason, PI selection was limited at low energies, as explained in Appendix A.1. Still, some contamination of X-ray events by the CCD system peak can be expected. For this reason, the spectrum above 30 Å was also excluded from the spectral fit (see Fig. 6). However, we were able to derive the nitrogen abundance by extending the fit range – for the sole purpose of determining that abundance – to 32 Å. That fit gives biased values for all other parameters, but the jump across the nitrogen edge at 30.8 Å is determined well.

Furthermore, we omitted small regions near the interstellar oxygen K-edge (22.7–23.2 Å) and iron L-edge (17.2–17.7 Å), for reasons explained in more detail in our discussion (Sects. 4.1.2–4.1.3; essentially the presence of molecules that affect the fine structure of the edge). As the ISM abundances are mainly determined from the depth of the absorption edges, ignoring these small regions does not affect the basic outcome of our analysis.

3.3. Results of the spectral fits

We have obtained a fit using model A outlined in Sect. 3.2 with a χ^2 of 2341 for 1316 degrees of freedom. The fit is shown in Fig. 6 and the parameters are given in Table 2. The fit residuals over the fitted range have – on average – an intrinsic systematic scatter of 1.8% and a random noise component of 1.9%, yielding a total scatter of 2.6%. Therefore, the typical systematic uncertainty in our model is less than 2%. The higher deviations outside the fitted range can be simply understood as we already discussed in Sect. 3.2.

For our alternative model B that includes dust, we list the best fit parameters also in Table 2. We have tried to leave the basic dust parameters free in our fits: grain mass density ρ, minimum and maximum size $a_{\rm min}$ and $a_{\rm max}$, and the size distribution index p. However, our fit is not very sensitive to these parameters, and therefore we have kept them to their default values listed in Sect. 3.2.

3.3.1. Search for hot gas

The fit residuals near 21.6 Å (Fig. 7) and 19.0 Å (Fig. 7), where we would expect the 1s–2p transitions of O VII and O VIII respectively, show some evidence of additional weak absorption features. We have determined the formal equivalent width of these features by adding narrow absorption lines to the model (but broadened due to the spatial extent of Crab as seen by RGS).

For the O VII line, we find a formal equivalent width of 9 ± 4 mÅ, and for O VIII 7 ± 2 mÅ if the line is narrow. For O VIII the feature looks somewhat broader; if we allow the width of the line to vary, we find a higher equivalent width of 18 ± 4 mÅ, but this requires a high velocity width (Gaussian $\sigma = 5000$ km s^{-1}).

For consistency, we have checked a Chandra LETGS spectrum of the Crab pulsar (Obsid 759), and found a formal equivalent width of the O VII line of 7 ± 17 mÅ, consistent with our RGS measurement.

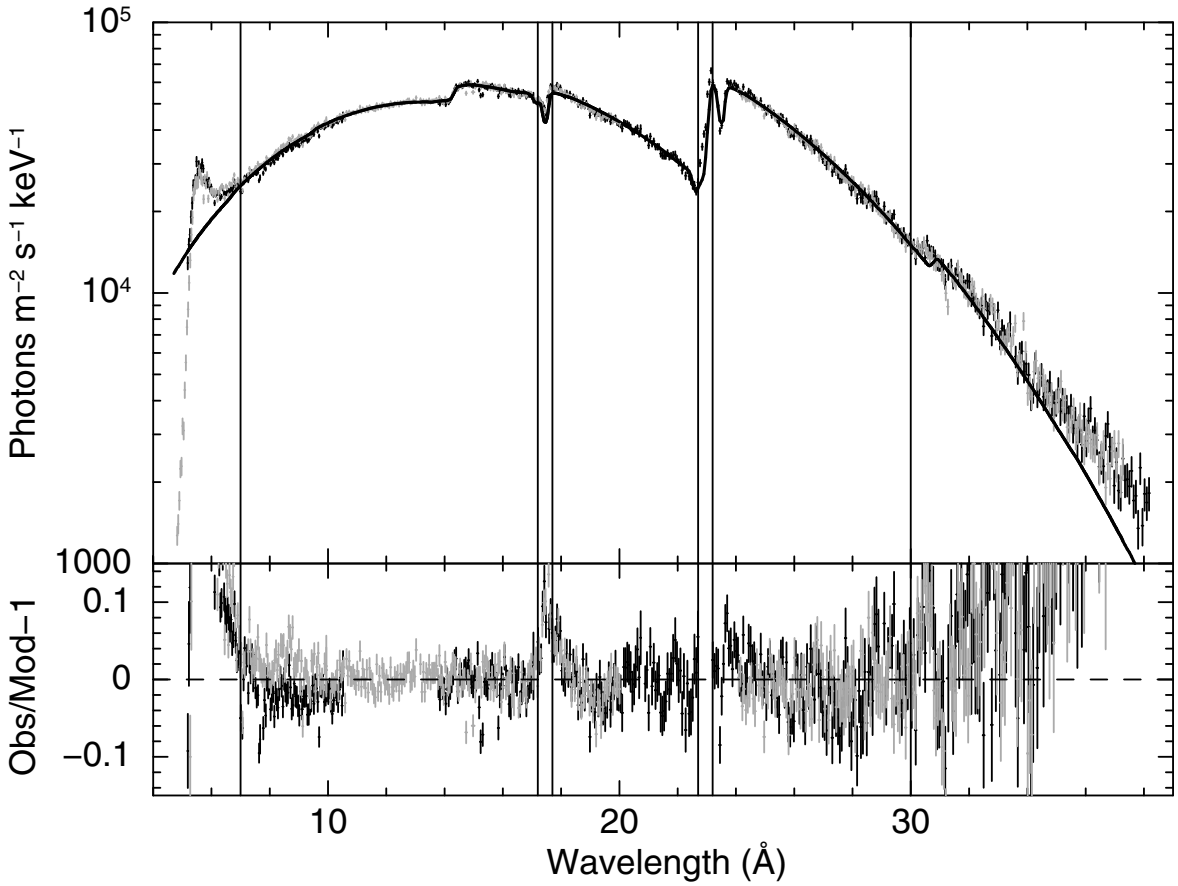

Fig. 6. Best fit RGS spectrum of the Crab nebula using model A. The fit was restricted to the 7−30 Å range (indicated by the vertical lines), excluding two small regions near the O I K-edge and Fe I L-edge (also indicated by vertical lines). However in the plot we show the full data range. Single and double CCD readout modes have been combined, but RGS1 (dark colour) and RGS2 (light colour) data are shown separately. *The upper panel* shows the fluxed RGS spectrum (but at the original spectral resolution of the data, including spectral broadening due to the spatial extent of the nebula). For clarity reasons we plot the flux in keV units along the y-axis, which reduces the dynamical range along that axis significantly. *The lower panel* shows the relative fit residuals.

4. Discussion of the absorption spectrum of Crab

4.1. Fine structure near absorption edges

Our fits (Fig. 6) clearly show strong absorption edges of neutral O, Fe and Ne. Other edges are weaker (like Mg at 9.47 Å and N at 30.77 Å). In principle, the neutral Si edge at 6.72 Å is also in the RGS band and is expected to have an optical depth of 0.017; however, it is in the part of the spectrum where our fits become poor and also any uncertainty related to the instrumental Si edge will contribute to its systematic uncertainty. Therefore we will not discuss Si further in our paper. We will discuss here in more detail the edges of Ne, Fe, and O.

4.1.1. Neon K-edge

The Ne-edge is clearly detected in the data (Fig. 7). The optical depth τ of the edge is 0.15. Nearby is the L_1 edge of neutral iron, but that edge is much weaker: $\tau = 0.010$. Recently, Juett et al. (2006) have studied the fine structure near the neon K-edge and iron L-edge using Chandra HETGS spectra of X-ray binaries. The spectral resolution of the HETGS (0.01−0.02 Å), combined with the point source nature of these objects, gives them effectively a 10−20 times higher spectral resolution than our Crab spectrum (extended source). For Ne I, in addition to the pure absorption edge, there is the series of 1s−np transitions ($n > 2$ because the 2p shell is completely filled for Ne I). According to the model of Juett et al., the 1s−3p line is at 14.295 ± 0.003 Å, and this line is strong enough that the effective K-edge of neon shifts towards this wavelength. For the true edge[1], we used the value of 14.249 Å. When we leave it as a free parameter, the best fit value for the edge is 14.231 ± 0.013 Å. This low shift is most likely caused by our neglect of the Rydberg series for $n > 5$ in our absorption model.

The K-edges of O VIII and Ne I differ only by ~0.02 Å. With our current effective spectral resolution for Crab, we cannot resolve these edges. However, as we show later (Sect. 4.3.1) the amount of hot gas in the line of sight is small enough to be neglected.

4.1.2. Iron L-edge

We have already seen that the L_1 edge of Fe I is very weak, and we will not discuss that edge further. The predicted depth of the L_2 and L_3 edges for our best-fit model A are only $\tau = 0.027$ and $\tau = 0.056$, respectively. At a first glance this looks contradictory to the deep features seen in Fig. 7. The difference is due to the presence of strong inner-shell line transitions (for example

[1] The definition of "edges" by Juett et al. is non-standard. They define the edge where empirically the flux drops; we keep here the more formal definition of the series limit of the absorption lines.

Table 2. Best fit parameters.

Parameter[a]	Model A pure gas curv. corr.	Model B gas & dust curv. corr	Model C pure gas no curv. corr
χ^2	2341	2327	2366
d.o.f.	1316	1315	1316
$f(5)$[b]	1.056 ± 0.009	1.055 ± 0.009	1.035 ± 0.009
$f(40)$[b]	0.746 ± 0.016	0.762 ± 0.016	0.854 ± 0.019
column densities[c]:			
H I[d,e]	31 750 ± 220	9700 ± 1700	31 280 ± 220
H I[d,f]	–	22 300 ± 1800	–
H I[d,g]	31 750 ± 220	32 060 ± 220	31 280 ± 220
H II[h]	1752 ± 4	1752 ± 4	1752 ± 4
N I	2.67 ± 0.24	2.72 ± 0.24	2.48 ± 0.25
O I	19.28 ± 0.18	19.83 ± 0.22	19.23 ± 0.18
O II	0.23 ± 0.14	0.25 ± 0.15	0.20 ± 0.14
Ne I	4.69 ± 0.21	4.66 ± 0.21	4.74 ± 0.21
Ne II	0.46 ± 0.25	0.52 ± 0.24	0.64 ± 0.25
Mg I	1.14 ± 0.28	1.20 ± 0.28	1.13 ± 0.28
Mg II	0.00 ± 0.09	0.00 ± 0.10	0.00 ± 0.09
Fe I	0.65 ± 0.05	0.77 ± 0.04	0.65 ± 0.05
Fe II	0.23 ± 0.06	0.14 ± 0.04	0.26 ± 0.07

[a] Error bars are all 1σ for one interesting parameter.
[b] $f(5)$ and $f(40)$ are the values of the effective area scale factor $f(\lambda)$, Eq. (5), at 5 and 40 Å.
[c] Ionic column densities are given in units of 10^{21} m^{-2}. The column densities of all metals include all phases (dust and gas).
[d] H I includes in the cross section contributions from neutral He, C, Si, S, Ar, Ca and Ni assuming proto-solar abundances for these elements.
[e] For the pure gaseous phase only.
[f] For the gas & dust mixture with proto-solar abundances added to the pure gaseous phase above.
[g] Total column: sum of contributions listed as *b* and *c*.
[h] For H II the column is derived from the pulsar dispersion measure assuming that all free electrons originate from hydrogen (see text).

2p−3d excitations). Such transitions have first been identified in an astrophysical source by Sako et al. (2001), and have subsequently been incorporated in our absorption models in SPEX. Those transitions cause the two deep absorption troughs at 17.1 and 17.4 Å. They are also visible in the HETGS data of Juett et al. (2006), at similar wavelengths. At our effective spectral resolution it is not possible to separate the inner shell transitions of Fe I from those of Fe II; the blends for these ions almost coincide. Therefore, the difference between the absorption by both ions is mainly derived from the different location of the absorption edges (see Fig. 7).

Similar to the case of the neon edge, also here possible contamination by highly ionised oxygen must be considered. Within our effective resolution, the O VII K-edge is close to the Fe II L_3 edge (Fig. 7). Our model gives an optical depth of 0.019 for this Fe II L_3 edge, while the O VII edge has a depth of at most 0.002. Thus, contamination of the iron edge by highly ionised oxygen is less than 10%, well below the statistical uncertainty on the Fe II column density.

Although the column density of Fe is determined well from the jump across the absorption edge, our fit is not optimal. At the long wavelength side of the edge, between 17.5−18.0 Å, there is excess flux of the order of 5%. This excess extends downwards to 17.1 Å. Adopting a ∼5% higher continuum between 17−18 Å, our absorption model provides a reasonable fit. Note that our model B with dust provides a slightly better fit in the absorption lines compared to model A; this is due to the high opacity of the

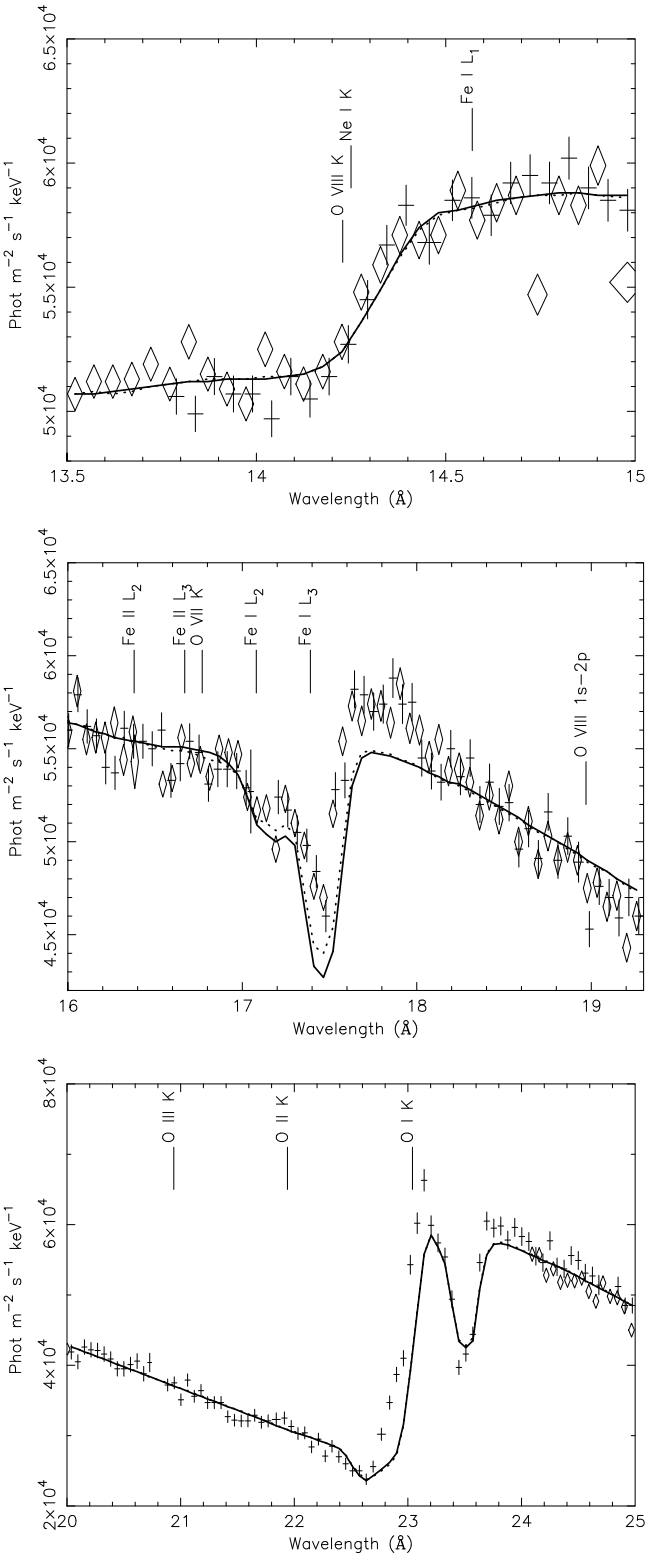

Fig. 7. Blow-up of Fig. 6 near the Ne I K-edge (*top*), Fe I $L_{2,3}$-edge (*middle*) and O I K-edge (*bottom*). Crosses: RGS1; diamonds: RGS2; solid line: model A (no dust); dotted line: model B (with dust).

lines, which results into stronger shielding effects by dust grains, and therefore to a relatively lower line to continuum opacity than for the pure atomic case.

The 5% amplitude of the excess is much higher than any uncertainties in our cross-dispersion correction factor, excluding therefore an origin in uncertainties of dust scattering near the

iron edge. As Crab has a rather smooth synchrotron continuum, we do not expect such broad features to be present in the intrinsic Crab spectrum.

It is striking, however, that several of the fits of Juett et al. (2006) to spectra of X-ray binaries have excess flux of a similar magnitude just at the long wavelength side of the Fe edge, similar to our case (for example Cyg X-1). Although their features look a little sharper, convolving them with the spatial/spectral response of our Crab observation would yield similar features.

The instrumental fluorine K-edge near 17.8 Å is determined well from higher resolution RGS spectra of point sources with low interstellar absorption columns. Those spectra do not show similar residuals. Hence we can exclude an origin of the excess in the instrumental F K-edge.

Finally we note that it is unlikely that this excess is due to line emission from a supernova shell. Seward et al. (2006), using Chandra data, have derived an upper limit to the luminosity of such a shell of 2×10^{27} W. The observed excess with RGS, when fitted with a Gaussian profile, has a flux of 109 ± 8 ph m^{-2} s^{-1}, at a mean wavelength of 17.53 ± 0.03 Å and with σ = 0.57 ± 0.08 Å. At the distance of Crab, and correcting for foreground absorption, this corresponds to a (line) luminosity of 2.4×10^{27} W, almost equal to the upper limit to the total X-ray luminosity of any shell. Moreover, RGS cannot see all flux from such a shell unless the radius is less than 2.5′. For such a radius, the maximum wavelength shift observed with RGS due to the spatial extent of the emission is 0.35 Å. There are no strong line transitions close enough to explain the emission. For example, if the emission would be O VIII Lyα emission at 18.97 Å, it should be located about 10′ from the Crab pulsar.

4.1.3. Oxygen K-edge

The oxygen K-edge clearly is the strongest feature of the spectrum, with a jump of a factor of 2 across the edge. The 1s−2p absorption line is reproduced well by our fit. However, in our original fit the edge energy, for which we used a value of 23.045 Å, clearly seems to be off. Making it a free parameter, we find a best-fit wavelength of 22.917 ± 0.008 Å, a shift of −0.128 Å. This does not mean that the edge itself is shifted. Two effects may cause the discrepancy.

First, we use the continuum cross sections of Verner & Yakovlev (1995). In this calculation, there is no fine structure at the edge, which is located at 538 eV (23.045 Å). The edge, however, has at least two strong sub-edges at the ^2P series limit (22.567 Å), and ^4P series limit (22.767 Å). Furthermore, the calculated wavelengths of the absorption lines that we use cannot be calculated more accurately than typically 10−30 mÅ. Only the strongest transition (1s−2p) was adjusted empirically to observed values. All this causes significant uncertainty in the adopted absorption model for atomic oxygen. We do not attempt to resolve this problem here but refer to a forthcoming paper (de Vries et al. 2008) for a more extensive discussion of the K-shell absorption structure in X-ray sources; also see the discussion in Paerels et al. (2001) and Juett et al. (2004).

Secondly, we note that in our fit with model B, with our adopted oxygen dust depletion factor of 0.4 for the dust+gas mixture, the total fraction of oxygen bound in dust is 28% (as there is also a pure gaseous component). This number is quite uncertain as it depends on our adopted dust depletion factor. Oxygen bound in minerals or dust grains has a clearly different fine structure near the edge than atomic oxygen; see for instance the many examples in van Aken et al. (1998). This changes the absorption structure for the chemically bound oxygen population significantly.

As the O II and O III edges are separated well from the O I edge, the high spectral resolution of RGS allows us to put tight upper limits on the amount of ionised oxygen. No strong edges of these ions are seen in the spectrum.

Figure 7 also shows a small depression near 21.6 Å, the wavelength of the strong resonance line of O VII. We discuss that further in Sect. 4.3.1.

Finally, based on our work on blazars as described in Paper III (Kaastra et al. 2009a), we estimate that the systematic uncertainty on the neutral oxygen column in Crab due to the uncertainty in the instrumental oxygen edge is less than 1%.

4.2. Column densities of the cold gas

From the column densities obtained from Table 2 we see that the absorbing medium is mostly neutral, except for iron, for which we find a significant ionised contribution. Column densities towards Crab have also been measured using UV and optical spectroscopy by Sollerman et al. (2000, S00 hereafter). They derived column densities based on a Doppler width of 1 km s^{-1}. For such a low velocity broadening, the lines are strongly saturated and hence the statistical uncertainty on the column densities are relatively high, despite significant line detections.

S00 obtained a neutral hydrogen column density of (3.0 ± 0.5) × 10^{25} m^{-2}, fully consistent with our more precise value of (3.18 ± 0.02) × 10^{25} m^{-2} for model A or (3.21 ± 0.02) × 10^{25} m^{-2} for model B.

There are 4 ions in common between our work and S00: O I, Mg I, Mg II and Fe II. For O I and Fe II, the column densities agree within the statistical errors of a factor of 2 and 4, respectively. However, for Mg I and Mg II there is a bigger difference. S00 find a Mg II/Mg I ratio of 5, with an uncertainty of a factor of 2, while we find a ratio less than 0.1. The total magnesium columns however agree: we find (1.1−1.2 ± 0.3) × 10^{25} m^{-2} for models A and B respectively, compared to $(0.7^{+0.7}_{-0.4}) \times 10^{25}$ m^{-2} for S00.

The different ratio appears puzzling but can be understood as follows. First, the Mg I and Mg II edges are close, at 9.48 and 9.30 Å. The optical depth of the Mg I edge (our deepest Mg edge) is about 0.02. In this region of the spectrum (see Fig. 6), there is a small difference between the RGS1 and RGS2 data, at the 1% level. It is therefore easy to get systematic errors at this level. While the total magnesium column is rather robust (as it measures essentially the jump across the combined nearby Mg I and Mg II edges), discriminating between both ions is harder because this depends solely on the small data stretch between 9.30−9.48 Å.

We therefore believe that a higher Mg II/Mg I ratio than reported by us is quite well possible, but that our total magnesium column is rather secure. Such a higher ratio would also be consistent with the enhanced degree of ionisation of iron.

4.3. ISM constituents

For a proper discussion of abundances, the different phases of the ISM should be taken into account. Near the Sun, we have the following components (see the recent overview of the ISM by Ferrière 2001, for more details):

1. hot ionised gas (~10^6 K);
2. warm ionised gas (~8000 K);
3. warm atomic gas (6000–10 000 K);

4. cold atomic gas (20–50 K);
5. molecular gas (10–20 K);
6. and dust.

We consider these components in more detail below.

4.3.1. Hot ionised gas

In general, the presence of hot gas in the line of sight towards any X-ray source is most easily seen using high spectral resolution measurements of the associated absorption lines. This is because in general the column densities of highly ionised gas are relatively low and therefore the absorption edges are weak, while the absorption lines still may be visible.

X-ray absorption due to the presence of hot gas in our Galaxy has been reported before. Yao & Wang (2006) analysed Chandra grating spectra toward the bright low mass X-ray binary 4U 1820-303, which has a neutral hydrogen column density of 1.5×10^{25} m^{-2}, half of the value towards Crab. In 4U 1820-303, these authors find equivalent widths for the O VII and O VIII 1s−2p absorption lines of 40 ± 12 and 19 ± 6 mÅ, respectively. These values are much higher than the values that we obtain for Crab (Sect. 3.3.1), of 9 ± 4 and 7 ± 2 mÅ, respectively.

Due to the weakness of the O VII and O VIII absorption lines toward Crab, it is hard to estimate the associated column densities. If the velocity dispersion of the gas $\sigma_v = 180$ km s^{-1}, the value found by Yao & Wang toward 4U 1820-303, then the column densities of O VII and O VIII are $(8 \pm 3) \times 10^{19}$ and $(2.6 \pm 0.9) \times 10^{19}$ m^{-2}, respectively, 2.5 and 10 times below the values towards 4U 1820-303. The optical depth at the K-edge of these ions is then less than 0.002, and therefore the neglect of these ions in our analysis is justified. For solar abundances, and assuming that all oxygen of the hot gas would be in the ionisation stage of O VII or O VIII, the total hydrogen column density of the hot gas would be 2×10^{23} m^{-2}, less than 1% of the neutral hydrogen column density.

Unfortunately, we do not have a good constraint on σ_v. If σ_v were substantially lower than 180 km s^{-1}, much higher columns would be required. We have worked this out as follows. We made a fit to our spectrum adding columns of O VII, O VIII and Ne IX to our model in the form of an additional *slab* component. These ions are dominant X-ray opacity sources for typical temperatures of a million K. Surprisingly, our fit improves significantly ($\Delta\chi^2 = 88$). The improvement is produced mainly by the inclusion of the absorption lines as well as fine tuning of the continuum, in particular near the neon and iron edges, although the ∼5% excess emission near the Fe-L edge still remains. Because the O VII K-edge is close to the Fe II $L_{2,3}$ edges (see Fig. 7), the fit reduces the Fe II column to zero in exchange to the O VII column. In a similar way, Ne I is reduced in favour of O VIII, also because both edges are so close (Fig. 7). Still the overabundance of neon remains.

However, this model is not acceptable because of other reasons. First, the total column of highly ionised oxygen (O VII and O VIII) is high: 5×10^{21} m^{-2}. Combined with the ionised hydrogen column deduced from the electron density (determined from the pulsar dispersion measure, see Sect. 4.3.2), an overabundance of oxygen of 6 times solar is required. This overabundance is even a lower limit if a significant fraction of the ionised hydrogen is associated with warm (10^4 K like) gas instead of hot (10^6 K like) gas. The most important problem with this model is, however, that the required velocity dispersion of the gas is $\sigma_v < 3$ km s^{-1}, far below the thermal velocity of the hot gas. If the hot gas is predominantly in collisional ionisation equilibrium, then for a typical temperature of 10^6 K, the thermal velocity of oxygen ions is more than 20 km s^{-1}.

Of course, we can solve this problem by accounting properly for the thermal width of the lines. We have done this by replacing the additional *slab* component by a *hot* component with solar abundances. Additional free parameters are the total hydrogen column density, the temperature and the velocity broadening σ_v to be added in quadrature to the thermal width of the lines. This model yields only a modest fit improvement over the original model without hot gas: $\Delta\chi^2 = 23$. We find a typical temperature of 2−3 million K and a hydrogen column of 5×10^{23} m^{-2}, almost two orders of magnitude below the column density of neutral hydrogen. Accordingly, the optical depths of the strongest oxygen edges for this component are at most 0.001, and there is no significant change to any of the parameters for the cold absorption component.

In summary, we conclude that some hot gas may be present in the line of sight towards Crab, at a level of a percent of the neutral hydrogen column. Typically, the amount of hot gas towards Crab is less than $N_H \lesssim 5 \times 10^{23}$ m^{-2}. This is small enough that neglecting it does not affect our results for the cold phase or the calibration of the Crab spectrum.

As the abundances in the hot ionised gas may be slightly different from those of the colder components (Yao & Wang 2006), we exclude this hot component explicitly from our abundance analysis.

4.3.2. Warm ionised gas

Pulsar dispersion measurements (for example Lundgren et al. 1995) yield a total electron column density of $(1.752 \pm 0.003) \times 10^{24}$ m^{-2}, where the error is dominated by the monthly fluctuations of this number, probably caused by the Crab nebula itself (Isaacman & Rankin 1977). As this electron column density is high compared to the hot ionised gas column density, most of the free electrons must be produced by the warm ionised gas. For the typical conditions prevailing in that medium, most of these electrons come from hydrogen. Hence, we use the electron column density as an estimate for the H II column density.

The other elements in the warm ionised gas are either neutral or singly ionised, and they are accounted for in our absorption model, although we cannot distinguish between the neutral atoms in this gas phase and those in the cold and warm atomic gas.

4.3.3. Cold and warm atomic gas

These two gas phases mainly contain neutral atoms. In the X-ray band, they are hard to distinguish, the main difference being the thermal line width. These are hard to measure, however, as the associated absorption lines are strongly saturated. Therefore we discuss the combined abundance of both phases, and also include the neutral and singly ionised atoms from the warm ionised gas in this component.

4.3.4. Molecular gas

Special attention needs to be paid to molecular hydrogen (H_2) here, as it is the main molecular X-ray opacity source.

The distribution of molecular gas in the Galaxy is very irregular and depends strongly upon the line of sight. It has a relatively high concentration closer to the centre of the Galaxy and is less important further outwards. In the local ISM, about

20−25% of the hydrogen is in its molecular form (Savage et al. 1977), and it is this value that is used as default in for example the absorption model of Wilms et al. (2000), although these authors warn the user to take care of such spatial variations. Over the X-ray band, the H_2 opacity per hydrogen atom is about $\sigma_{\rm mol}/\sigma_{\rm atom} = 1.42$ times higher than for H I (Wilms et al. 2000). Hence, for a mixture with a 20% molecular contribution, the effective hydrogen opacity should be 8% higher than for pure H I; ignoring this molecular component would therefore bias abundance determinations.

In our spectral model we have ignored molecules, so we need to justify this. We do this by determining R, the relative enhancement of the total opacity including molecules compared to the opacity of the same gas if it is fully atomic. R can be written as

$$R = \left(\frac{\sigma_{\rm mol}}{\sigma_{\rm atom}} - 1\right) \times \frac{n_{\rm mol}}{n_{\rm atom}} \times f_{\rm H} \qquad (6)$$

where here $n_{\rm mol} = 2n_{\rm H2}$ and $n_{\rm atom}$ are the number densities of hydrogen nuclei in molecular and atomic form, respectively. Furthermore, $f_{\rm H}$ is defined here as the effective opacity of hydrogen relative to the other metals in our X-ray spectrum.

For gas with solar composition, the contribution of hydrogen to the total opacity varies between 5% at 10 Å to 17% at 30 Å. A typical weighted average value for our Crab spectrum is ∼10%. As approximately half of the total opacity is produced by elements such as N, O, Ne, Mg and Fe for which we determine the column densities separately, we estimate $f_{\rm H}$ by comparing the pure hydrogen opacity to the total opacity produced by the elements that we tied to hydrogen using solar abundances. This leads to an estimated of $f_{\rm H} = 0.2$.

Crab lies in the direction of the Galactic anticentre, at a distance of 2 kpc. Therefore the fraction of H_2 is expected to be lower than the typical value of 20%. From the CO maps of Dame et al. (2001) (available through NASA's skyview facility), and using their conversion factor from CO equivalent width to H_2 column, we find $n_{\rm H2} < 5 \times 10^{22}$ m^{-2}. There is a molecular cloud with a higher column density of 10^{24} m^{-2} North of Crab, but it is more than 5′ away. Therefore, our best estimate is $n_{\rm mol}/n_{\rm atom} < 0.003$ (direct upper limit) or $n_{\rm mol}/n_{\rm atom} < 0.06$ (worst case scenario, if the cloud North of Crab would cover it).

Taking all these factors into account, we find $R < 0.42 \times 0.003 \times 0.2 < 3 \times 10^{-4}$. For the worst case scenario with $n_{\rm mol}/n_{\rm atom} < 0.06$, still $R < 0.005$. Therefore, we can completely ignore the role of molecular gas in our line of sight.

4.3.5. Dust

Dust in the line of sight towards Crab or any other X-ray source has two effects: scattering and absorption of X-rays.

Scattering does not destroy photons but merely redistributes them into a halo around the source. Recently, Seward et al. (2006) have studied the dust scattering halo of Crab using Chandra imaging. They conclude that the total column density of scattering material (dust and associated gas) is $1.7-2.2 \times 10^{25}$ m^{-2} for their best fit model, and 2/3 of that value for an alternative model. Most of this can be modelled to be in a smoothly distributed component between us and Crab, while 10−25% of the scattering material is in a single structure at a distance of ∼100 pc from the Sun, perhaps associated with the boundary of the local hot bubble. Surprisingly, the total column density that Seward et al. (2006) find is less than the column derived from X-ray absorption measurements. This may indicate a relative low abundance of dust towards Crab.

Table 3. Wavelengths of absorption lines, all in Å.

Constituent	Oxygen main line	Iron main line	Iron 2nd line	Ref.
Ferrous, Fe^{2+}		17.498	17.196	a
Olivine	23.26			b
Ferric, Fe^{3+}		17.456	17.130	a
Hematite	23.43			b
Atomic O I	23.508			c
Atomic Fe I		17.453	17.142	d
Crab	23.466 ± 0.009	17.396 ± 0.009	17.120 ± 0.016	e

[a] van Aken & Liebscher (2002), corrected by −0.019 Å following Juett et al. (2006); [b] van Aken et al. (1998); [c] Juett et al. (2004), from Chandra spectra; [d] Behar et al. (2001), HULLAC calculations; [e] present work.

The amount of dust inside Crab is relatively small, and can contribute only 1−2% to the total column density towards Crab. This can be derived from infrared observations: Temim et al. (2006) estimate that Crab contains about 0.004−0.010 $M_\odot$ of graphite or 0.006−0.015 $M_\odot$ of silicates, in order to explain the thermal dust emission seen at 70 μm. Assuming a constant density sphere with radius 2′, the total carbon column of the dust within Crab (in case of graphite) would be $0.7-1.8 \times 10^{20}$ m^{-2}, and in case of silicates (assuming for simplicity olivine or Fe_2SiO_4) the silicon column would be $0.6-1.6 \times 10^{19}$ m^{-2}. In both cases, this corresponds to 1−2% of the total interstellar column. Hence we will ignore this component.

Apart from scattering, dust also absorbs X-rays. There are two main differences between the absorption properties of atoms contained in dust and free atoms. First, the absorption edges and lines in bound atoms are slightly different, due to the chemical shifts. Secondly, the effective absorption cross section can be less due to shielding in grains.

Unfortunately, our spectral resolution is not very high due to the extended nature of the Crab emission. Therefore it is hard to measure accurately the location of absorption lines. However, our data still contain some usefull information on that.

In Table 3 we compile our current knowledge about the dominant absorption lines in different constituents, and compare it with the observed centroids as measured in our Crab spectrum. These observed wavelengths were obtained by ignoring the absorption lines in our best fit model and fitting them instead with narrow absorption lines. Olivine ($Mg_{2-x}Fe_xSiO_4$) is one of the best known examples of a ferrous, and hematite (Fe_2O_3) of a ferric compound.

If we consider neutral oxygen, then the observed absorption line centroid suggests approximately equal contributions from atomic and ferric iron (Table 3). Such a mixture also gives good agreement with the secondary iron line blend at 17.12 Å, and is also in agreement with the ∼30% of oxygen bound in dust derived from our model B. There is only disagreement with the main iron line blend at 17.40 Å. Clearly, both ferric and atomic iron have their predicted line closer to the observed centroid of this blend than ferrous iron, but none of them agree fully. It may be that the predicted wavelengths by Behar et al. (2001) are slightly off, as these lack detailed experimental validation; however, their calculations agree within a few mÅ with other calculations (Raassen & Kaastra, private communication, as quoted by Behar et al.). We suggest that the dust line of sight towards Crab is dominated by ferric compounds.

The second difference in absorption properties of dusty atoms compared to free atoms is the shielding of atoms in dust

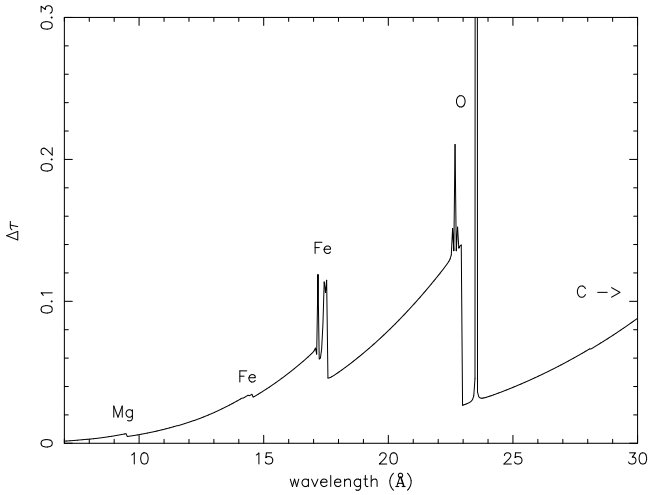

Fig. 8. Difference in optical depth for an equivalent hydrogen column density of 3.16×10^{25} m^{-2}, for dust with depletion factors as given by Wilms et al. (2000), compared to the same material but dissolved into free atoms. The most important spectral features are indicated.

Table 4. Abundances, all relative to the proto-solar values of Lodders (2003).

Element	Model A pure gas curv. corr.	Model B gas & dust curv. corr	Model C pure gas no curv. corr
H	≡1	≡1	≡1
N	1.00 ± 0.09	1.01 ± 0.09	0.95 ± 0.10
O	1.012 ± 0.014	1.030 ± 0.016	1.022 ± 0.014
Ne	1.72 ± 0.11	1.72 ± 0.11	1.83 ± 0.11
Mg	0.82 ± 0.21	0.85 ± 0.21	0.82 ± 0.21
Fe	0.76 ± 0.07	0.78 ± 0.05	0.79 ± 0.07

grains. The shielding leads to effectively lower opacity per atom. This is illustrated in Fig. 8. At the oxygen edge, the difference can be up to 14%. In practice, the effects of inclusion of dust in the model are not as dramatic as shown here. The reason is that one can always adjust the abundances slightly in order to correct for the highest changes in the depth of the edges. Therefore, despite the significance of the different dust cross sections, the total opacity is similar to that of pure atomic gas and this is the main reason of the only modest improvement of the fit with model B compared to model A. It also explains why it is hard to use our data to constrain the properties of the dust – density, grain size, etc.

However, the most robust statement we can make about the dust is the associated column density. From Table 2 we see that the column density of the gas associated with the dust is about 70% of the total column density, and its value of $(2.23 \pm 0.18) \times 10^{25}$ m^{-2} is in good agreement with the value derived by Seward et al. (2006) based on modelling of the dust scattering halo. Thus, we confirm their finding of a reduced dust column towards Crab as compared to a standard gas/dust mixture.

4.4. ISM abundances

We have determined the abundances of all elements for which we have reliable individual column density measurements. These abundances are shown in Table 4. They include all phases of the ISM except for the hot ionised gas. We see that the abundances do not depend significantly on the inclusion of dust in our models.

Interestingly, the abundances that we derive for most elements except for neon are close to the proto-solar abundances of Lodders (2003) that we used as a reference. Oxygen and nitrogen fully agree with the proto-solar abundances, while the magnesium and iron abundances are only slightly lower.

The only exception to this general abundance pattern is neon. It has an overabundance of ∼1.7. Antia & Basu (2005) and Drake & Testa (2005) recently argued that the solar neon abundance should be higher. Based on measurements of neon to oxygen in stars, Drake & Testa derive a Ne/O number ratio of 0.41. Relative to the proto-solar values (Ne/O number ratio 0.15), this would imply an overabundance of neon compared to oxygen of 2.6. Clearly, we find an enhanced neon abundance, but only 2/3 of the value of Drake & Testa. In fact, our Ne/O number ratio of 0.26 ± 0.02 is in excellent agreement with recent measurements of the abundances in the Orion nebula (Ne/O = 0.24 ± 0.05, Esteban et al. 2004) and of B-stars in that nebula (Ne/O = 0.26 ± 0.07, Cunha et al. 2006).

4.4.1. The role of carbon

As the carbon K-edge is longwards of the RGS wavelength band, it is difficult to estimate the carbon abundance from our measurements. However, as carbon contributes approximately 10% to the total opacity below the oxygen K-edge, it is potentially an important factor to take into account.

Our best-fit model predicts a total carbon column density of 9.2×10^{21} m^{-2} for our adopted proto-solar abundances. S00 found from their optical and UV spectroscopy a column density of atomic C I of 8.5×10^{21} m^{-2}; however the error bars of a factor of 2 allow a range between $4–16 \times 10^{21}$ m^{-2}. In addition, they found a C II column of 14×10^{21} m^{-2}, but here the error bars are a factor of 3, allowing a range between $5–50 \times 10^{21}$ m^{-2}. Given these numbers and the fact that a part of the carbon may be contained in dust, it is not very likely that the total column density of carbon is much below the proto-solar value.

To estimate the possible effects of a different carbon abundance, we have determined the best fit parameters in case the carbon abundance decreases to 0.7 times proto-solar, a similar value as the iron and magnesium abundance towards Crab. χ^2 of our fit then decreases by only 1.4, the hydrogen column density increases by 10^{24} m^{-2} or 3.2%, $f(5)$ increases by 0.3% and $f(40)$ decreases by 1.7%. We will use these numbers in our estimate of the systematic uncertainty in the RGS effective area.

5. Discussion of the effective area calibration of the RGS

We use our spectral fit to determine the absolute effective area of the RGS. This is achieved by determining the power-law correction factor $f(\lambda)$ from Eq. (5). As we described in Sect. 3.2, we determine this from the values of $f(\lambda)$ at 5 and 40 Å. From Table 2 we see that we can determine these numbers to an accuracy of 0.9 and 1.6%, respectively. The differences of these values for model A and B are not very high, at most 2% at the longest wavelengths.

The differences between model A and B with model C are much higher, as model C ignores the intrinsic curvature of the underlying continuum. But despite that the curvature correction at 40 Å (0.3 keV) is 22% (see Fig. 5), the enhancement of $f(40)$ is only 12%. This is because also other parameters in

Table 5. Summary of systematic and statistical uncertainties in the Crab spectrum.

λ Å	E keV	a	b	c	d	e	f	g	h	i	j	k	l	m
5	2.5	0.1	0.008	0.003	0.000	0.000	0.001	0.001	0.003	0.050	0.000	0.30	1.0	0.0031
7	1.8	0.1	0.011	0.005	0.000	0.003	0.002	0.002	0.000	0.010	0.001	0.04	0.022	0.0025
10	1.2	0.1	0.015	0.007	0.001	0.005	0.004	0.002	0.004	0.004	0.002	0.01	0.010	0.0025
15	0.8	0.1	0.019	0.010	0.001	0.000	0.006	0.010	0.008	0.005	0.002	0.00	0.008	0.0026
20	0.6	0.1	0.022	0.011	0.002	0.005	0.007	0.001	0.010	0.015	0.001	0.00	0.008	0.0045
25	0.5	0.1	0.024	0.013	0.002	0.005	0.009	0.003	0.012	0.020	0.001	0.00	0.008	0.0048
30	0.4	0.1	0.026	0.014	0.003	0.002	0.010	0.001	0.014	0.050	0.000	0.00	0.010	0.0090
type		c	c	c	c	u	c	c	c	u	c	u	u	u
$\Delta\alpha$		0.016	0.010	0.006	0.002	0.001	0.005	0.001	0.010	0.010	0.000	0.027	0.006	–
ΔA		0.100	0.019	0.010	0.001	0.001	0.004	0.005	0.004	0.003	0.002	0.005	0.002	–

Main power-law: [a] uncertainty in the K01 continuum model.
Curvature corrections: [b] a 50% change in the lower energy of the 2−8 keV range used for the normalisation of the Chandra data; [c] break size $\Delta\Gamma = 0.006$ at low E if a break (at 4 keV) is present in the Kuiper et al. data; [d] 0.5% of the absorption with $N_{\rm H}$ higher by 7.5×10^{24} m^{-2}; [e] numerical approximation of $f_{\rm c}(E)$ by (3).
Interstellar absorption: [f] systematic uncertainty in the dust model; [g] neglect of hot gas; [h] interstellar carbon abundance.
Instrumental corrections: [i] cross-dispersion correction; [j] pile-up correction for 2 CCD mode; adopts 5% uncertainty in a (2σ); [k] redistribution errors, estimated from difference fit residuals RGS1 and RGS2; [l] errors in the Chebychev polynomials used for the effective area correction; [m] typical combined RGS1/RGS2 statistical uncertainty for a full 1 Å wide bin.

the fit, in particular the neutral hydrogen column, have changed. The lower hydrogen column for model C partially compensates for the neglect of the continuum enhancement at low energies. Comparing model C with model A, none of the metallic column densities neither the abundances differ by more than 1σ. However, as we have shown in Sect. 2.5, there are strong arguments for applying the curvature correction. The systematic uncertainties on the correction as derived in Appendix B are significantly lower than the correction factor itself. We therefore propose to adopt our model B as the model that agrees best with all constraints.

The relatively low statistical uncertainties on $f(\lambda)$ are not the most important errors, however. There is a range of systematic factors that increase the uncertainty on $f(\lambda)$. The most obvious one is of course the 10% uncertainty on the absolute flux of the K01 intrinsic continuum that we used (Sect. 2). In another paper (Kaastra et al. 2009a) we show how we can reduce that uncertainty by combining the present results from our Crab analysis with observations of white dwarfs, for which we can determine the absolute X-ray flux with an accuracy of a few percent. Other systematic uncertainties cannot be reduced, however. In order to be able to assess the accuracy of our calibration, we need to make a quantitative assessment of all these systematic effects.

We estimate the known systematic uncertainties and present them in Table 5. We proceed as follows. For each relevant factor, we estimate its magnitude for a range of characteristic wavelengths, covering the RGS range between 5−30 Å. The systematic uncertainties are calculated by comparing the nominal fluxes with the derived fluxes when one of the relevant parameters is changed as described in Appendix B. These numbers are given in the table. Then we put each error in one of two specific categories.

For category "c", the systematic uncertainties at different wavelengths are more or less correlated. Example: the absolute flux of Crab is known to only 10%. Therefore, if the true flux of Crab at 5 Å differs by 10% from the value we adopted, it will differ by the same percentage for all other wavelengths. Taking this into account, we can assess for these "correlated" errors how they will affect the normalisation and slope of $f(\lambda) = A(\lambda/10)^{\alpha}$ by "fitting" the estimated systematic uncertainties (all having the same sign) directly to a power-law shape.

For category "u", the systematic uncertainties at different wavelengths are uncorrelated over the full RGS wavelength scale. A good example are the cross-dispersion corrections: as we use a combination of splines and power-law approximations, systematic errors are correlated over ranges between 0.5 and several Å, but there is no relation between the uncertainty at 7 Å to that at 30 Å. In those cases, we estimated ΔA from the typical slope and normalisation that we would obtain if the systematic uncertainties at different wavelengths had random signs. In general, for this type of uncertainty the direct effect on A and α is smaller than for correlated errors (category "c").

More details on the individual systematic uncertainties are given in Appendix B.

For completeness, we also list in Table 5 the statistical uncertainties on the Crab spectrum. As can be seen, these are low compared to the systematic uncertainties.

The main systematic uncertainty in the slope of our power-law correction (±0.027) originates from the redistribution errors (column (k) of Table 5). These uncertainties are mostly important below 10 Å. In principle, it should be possible to reduce these errors further, by a carefull analysis of a large sample of sources with different intrinsic spectral shape in the hard band. However, such an effort is beyond the scope of this paper. If we add up all other systematic uncertainties $\Delta\alpha$ on the slope in quadrature, except for the redistribution errors, the combined uncertainty is 0.020; the total rms systematic error is 0.034.

The main uncertainty on the absolute flux is – apart from the uncertainty in the K01 model listed in column (a) – the uncertainty in the lower energy used for the scaling of the Chandra spectra on the K01 model (column (b)).

In another paper (Kaastra et al. 2009a) we show how this uncertainty in flux can be reduced to about 3% by combining our results for Crab with white dwarf spectra. However, none of that analysis affects our present results on the Crab nebula.

6. Conclusions

We have studied the interstellar absorption towards Crab and determined the effective area of the RGS.

The interstellar line of sight towards Crab appears to be free of molecules and has a relatively low contribution of hot gas. It

contains only about 70% of the amount of dust expected from its absorption column, a conclusion that is in agreement with studies of the dust scattering halo by Seward et al. (2006). From the centroids of the dominant O-K and Fe-L absorption features, we conclude that gas and dust contribute roughly equally to these features, and that ferric iron is more abundant in the dust than ferrous iron.

We have determined the interstellar abundances with very high precision, the oxygen abundance with a relative accuracy even better than 2%. While oxygen and nitrogen are fully compatible with proto-solar abundances, we find slightly lower (~80% proto-solar) abundances for iron and magnesium, although for the last element we cannot exclude proto-solar abundances. On the other hand, neon is over-abundant by a factor of 1.7.

We can also put tight limits on the amount of singly ionised ions, thanks to our high spectral resolution. For instance, less than 2% of all oxygen is in the form of O II.

Concerning the calibration of RGS, we have accurately determined the effective area of this instrument. The relative accuracy of the effective area over the 7–30 Å band is equivalent to a power-law index uncertainty of about 0.03. The absolute effective area from our analysis is known to the same accuracy as the adopted continuum model spectrum of Crab, namely 10%. In a forthcoming paper (Kaastra et al. 2009a) we will show how that last uncertainty can be reduced to a few percent.

Acknowledgements. We thank Andy Pollock and his colleagues at ESOC for helpful comments on this paper. This work is based on observations obtained with XMM-Newton, an ESA science mission with instruments and contributions directly funded by ESA Member States and the USA (NASA). SRON is supported financially by NWO, the Netherlands Organization for Scientific Research.

Appendix A: Spectral extraction and response generation

A.1. Spectral extraction

Spectra and response matrices were created using the standard XMM-Newton data analysis system (SAS), version 7. The standard RGS pipeline "rgsproc" was used, but with a few adaptations explained below.

For point sources, the preferred method is to extract spectra that contain 95% of all photons in the cross-dispersion direction, and 95% of all photons in the pulseheight-wavelength (*PI*, "banana") regions. The response matrix then corrects for the missing flux fraction in both subspaces.

In our case, the situation is different. Crab is an extended source, with substantial emission wings containing ~10% of all flux in the ROSAT band. These wings are visible up to half a degree from Crab (Predehl & Schmitt 1995). Crab is therefore larger than the width of the RGS detector in the cross-dispersion direction, and also photons are spread over a larger region in the dispersion direction than for a point source. Moreover, Crab is bright and for some parts of the source pile-up of events cannot be neglected.

For these reasons, we extracted source spectra over the full width of the RGS detector (5.0 arcmin), and with a *PI* selection that contains 98% of the flux for each wavelength. Selecting 100% *PI* is not possible because then spectral order separation becomes impossible and at low *PI* values the selected range would fall below the lower threshold.

To prevent the broader *PI* selection to select background events from the CCD system peak, the *PI* selection was limited to *PI* values higher than 200 eV, well above the average system peak of around 100 eV. This made the *PI* selection narrower than 98% for wavelengths longer than 24.8 Å. This limitation of PI selection for a particular wavelength range is properly taken into account by the SAS processing system.

The response matrices that we used, however, were created for a selection of 95% in *PI* space and 95% in cross-dispersion space. These are the recommended values for point sources. We use those matrices because they are the best calibrated (see Sect. A.2), but we apply correction factors in the form of an *arf* file to this standard response matrix. Note that in general the standard SAS software produces only *rmf* matrices where the effective area has already been included. As our corrections go beyond the standard SAS, we have chosen here for the *arf* option.

The correction factors entering the *arf* are discussed in the next sections. All factors are multiplied to get the total area correction. They are:

1. 0.98/0.95, to correct for the 95% *PI* selection in the standard response matrix as compared to our actual 98% extraction.
2. 1.00/0.95, to correct for the 95% cross-dispersion selection in the standard response matrix as compared to our full detector (100%) extraction.
3. Dead time can be ignored. See Sect. A.3.
4. Pile-up correction $f_{\rm p}(\lambda)$. See Sect. A.4.
5. Vignetting of telescope and gratings. See Sect. A.5.
6. Loss of photons in the cross-dispersion direction due to the extended size of Crab $f_{\rm d}(\lambda)$. See Sect. A.6.

Finally, we need to correct for the extent of the source in the dispersion direction. This causes some spectral resolution degradation, but does not affect the effective area. This is discussed in Sect. A.7.

A.2. Standard response matrix

The standard response matrix contains an empirical correction factor for the nominal effective area for point sources (95% *PI* selection, 95% cross-dispersion selection). This empirical correction is based on all RGS spectra from Mrk 421, used as calibration source. We assume Mrk 421 to have a pure power-law spectrum of arbitrary power-law index and normalisation, which may change over time. We fit a power-law in the 10–25 Å wavelength range. The remaining part of the RGS spectrum is made to fit this spectrum using a set of low frequency Chebychev correction polynomials (up to order 12). A time-dependant correction is added assuming an increasing Carbon deposit on the RGS CCD's, with parameters based on the constant sources RX J1856.5−3754 and the Vela pulsar.

The standard SAS calibration now contains the Chebychev correction polynomials and carbon absorption model including the absolute effective area calibration based on the work described in this article. This latter correction was of course not used for this analysis, since this is a factor to be determined.

A.3. Dead time effects

For sources producing high count rates in the RGS such as the Crab nebula, many events are lost due to onboard processing constraints. When too many events are queued for on board processing or telemetry download, the processor will discard a number of CCD readouts (frames) to free its buffer. This will influence dead time, but will have no other consequences for the instrument response. The data reduction SAS software will take

the exact number of lost frames into account to compute the proper exposure time. Net result will only be a higher statistical noise than is expected on the basis of observing time only.

Since we selected 100% of the CCD width, events recorded during CCD frame transfer (out-of-time events) would still fall within the spatial selection window and hence do not contribute to any dead time.

A.4. Pile-up corrections

The brightest parts of the Crab nebula suffer from pile-up in the spectrum. This is evident from a reduced count rate in observations with 8 CCDs readout as compared to single CCD readout mode. For a given CCD, the net exposure time per frame in k CCD readout mode is simply k times higher than the default integration time of 0.57 s.

It is difficult to make an exact model for the pile-up. In general, any photon hitting the detector may give a signal either in a single pixel or in more than one pixel, with a range of many possible patterns. Within the same (time) frame, a second photon may hit the same or a neighbouring pixel, with its own pattern. The combined number of possible patterns is large, and the electronics, on-board and ground software treat each combination differently, also depending on the energy of both photons.

Therefore we create an empirical pile-up model. We define μ to be the expected number of counts per frame per pixel in single CCD readout mode (in the absence of pile-up). This number is obviously a function of the position on the detector. Even for sources as bright as Crab, the count rates are moderate. The maximum value of μ for the Crab nebula is less than 0.004. Therefore, already double events are rare and we can fully ignore pixels with three or more events. We consider only the effect of pile-up on the first-order spectrum. In general, when a genuine 1st order photon hits a pixel, and within the same frame a second event (first, second order or even background) hits the same or a neighbouring pixel, several things may happen but all lead to a rejection of the event as a first order photon: it is either rejected completely, or seen as a second order event with twice the energy or alternatively as a background event. Accounting for pile-up, $\mu_{1,\mathrm{p}}$, the expected number of first-order events in a given pixel can be written as:

$$\mu_{1,\mathrm{p}} = \mu_1(1 - ak\mu) \qquad \text{(A.1)}$$

where μ_1 and μ are the expected first order and total counts/per pixel per frame without pile-up, k is the number of CCD's read-out and a is a constant that needs to be determined.

For each pixel and all CCDs we have estimated μ by averaging all counts over time and 7×7 pixels around the relevant pixel (in order to reduce the noise). Then we grouped the pixels together in groups with the same range of μ values, and determined the total number of first order counts for the group in each readout mode. The number of first order counts for different k, as a function of μ, were fitted to Eq. (A.1). An example is shown in Fig. A.1. We determined the weighted average of a from all CCDs. These values are 8.17 ± 1.17, 6.46 ± 0.30 and 6.41 ± 0.17, from a comparison of $k = 1$ with $k = 2$, $k = 4$ and $k = 8$, respectively. Combining these numbers, our best estimate of a is 6.45 ± 0.15.

There is no significant difference between the value of a for RGS1 and RGS2. As can be seen from Fig. A.1, at low count rates there is a small, unexplained, deficit of count rate ratio. Fitting the pile-up correction in Eq. (A.1) not to $(1 - ak\mu)$ but to $(b - ak\mu)$, we find that b is typically a few percent lower than 1.

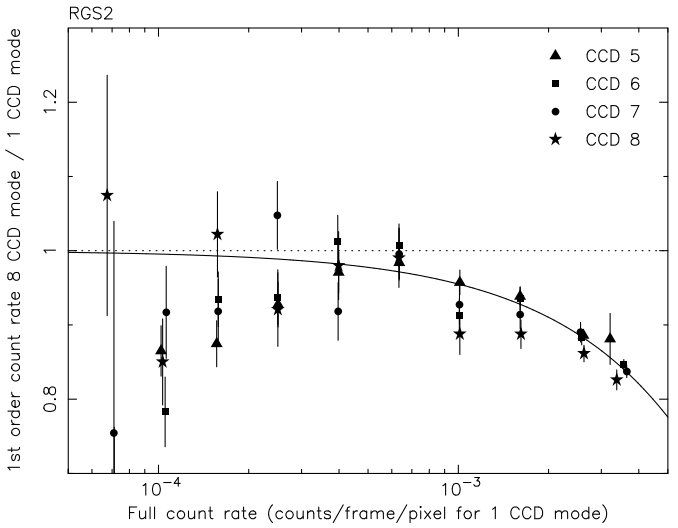

Fig. A.1. Ratio of first order count rates for the Crab nebula for 8 CCD mode as compared to single CCD mode, as a function of μ, the total number of counts per frame per pixel. We only show the results for CCD 5−8 of RGS2. The results for the other CCDs are similar. The curve indicates our best-fit model to Eq. (A.1).

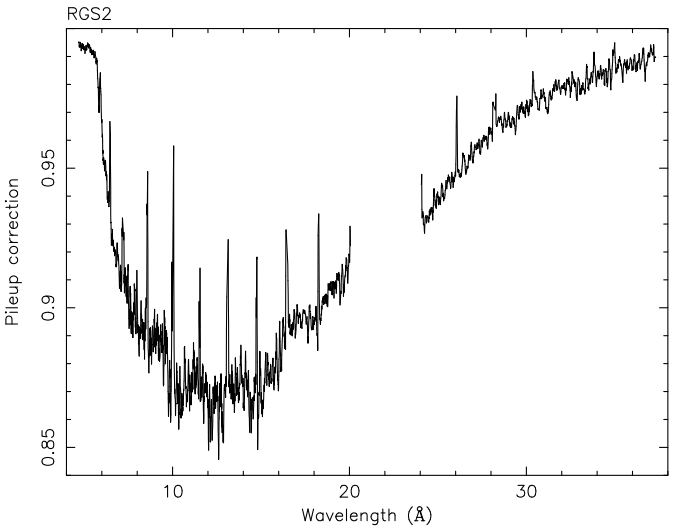

Fig. A.2. Pile-up correction for the Crab nebula observed with RGS2 in 8 CCD mode. Most of the spikes of lower pile-up are caused by CCD gaps and the central columns of CCDs.

However, as the fit is statistically driven by the brighter parts with high count rates (see the much lower error bars for high values of μ), the effect on the derived pile-up correction at high count rates is small. These brighter parts also dominate the total count rate of Crab. We estimate that the net effect on the integrated spectrum is equivalent to an enhanced uncertainty of ~0.45 in a, i.e. about 3 times the nominal statistical uncertainty in that quantity.

The value for a can also be used for observations of other targets, but it should be remembered that in our case it is defined for the 98% selection in energy space that we needed to use because of the extended nature of Crab.

The value of $a = 6.45$ is used to derive a wavelength-dependent correction factor for pileup $f_{\mathrm{p}}(\lambda)$, that we formally include in the effective area correction ("arf"). It is constructed by averaging $1 - ak\mu$ over the cross-dispersion direction, weighted by the observed first order count rate image corrected for pile-up.

In Fig. A.2 we show the arf correction for the Crab nebula. In 8 CCD mode, the maximum correction occurs at 1 keV and amounts to 14%.

A.5. Vignetting

The effective area of the RGS depends on the position of the source in the field of view. The standard effective area is calculated for a point source. For off-axis photons (either in the dispersion or cross-dispersion direction), the effective area differs due to vignetting of the telescope and obscuration and vignetting by the gratings. Crab is an extended source. For each energy band we have calculated the effective vignetting by multiplying a MOS image (see Sect. A.7) with the vignetting factor, including both telescope vignetting and grating obscuration. The average vignetting factor is 0.983, and to high accuracy it does not depend on energy within the RGS wavelength band. There is a weak increase of 0.2% in telescope vignetting from 7–25 Å caused by the enhanced size of Crab at longer wavelengths, and therefore more photons are off-axis. But this increase is compensated for by slightly lower grating obscuration at longer wavelengths. Therefore we multiply our effective area by this constant factor of 0.983.

A.6. Cross-dispersion correction

As Crab is an extended source and the RGS detectors have a limited width of about 5′ in the cross-dispersion direction, a fraction of all photons at each wavelength will not hit the detector. There are three causes for this loss: the extended emission of the nebula, dust scattering and additional scattering by the gratings of the RGS. In order to be able to use spectral models for the full Crab nebula, we need to account for this loss of events. We have implemented this as follows.

For our spectral fitting, we only use the on-source pointing, but we use our off-axis pointings in the cross-dispersion direction to estimate for each wavelength interval the fraction of the total flux that is lost in the central pointing. Unfortunately, the extent of the Crab nebula is even larger than our maximum off-axis angle (9.5′). Therefore we have to extrapolate the flux outside this maximum off-axis angle. In general, power-laws are good approximations for the dust scattering halo's at a given energy (Predehl & Schmitt 1995; Predehl & Klose 1996). Due to the asymmetry of the nebula and the grating scattering, we determine separate correction factors for both sides of the nebula. For the longest wavelengths, background becomes important and we have modelled this by subtracting an observation of the Lockman hole.

A typical example of our fits is shown in Fig. A.3. It is seen that the individual pointings do not fully coincide at their lowest and highest *chipy* positions. This is due to a combination of the outwardly decreasing flux of the nebula with the slightly asymmetric scattering of the gratings. However, the total correction factor is hardly affected by this slight lack of overlap, as we use two full off-axis observations on each side and our fit averages out these boundary effects.

We determined the cross-dispersion loss correction factor f_d (defined as the fraction of the Crab flux falling on the RGS detector for the central pointings) with the highest possible resolution. In practice this is achieved by dividing each CCD into 8 equal wavelength bins. However, in particular for the CCDs with lower count rates, we had to go to 4 or even 2 bins per CCD in order to obtain accurate values. We show the measured correction factors f_d in Fig. A.4. The following should be noted.

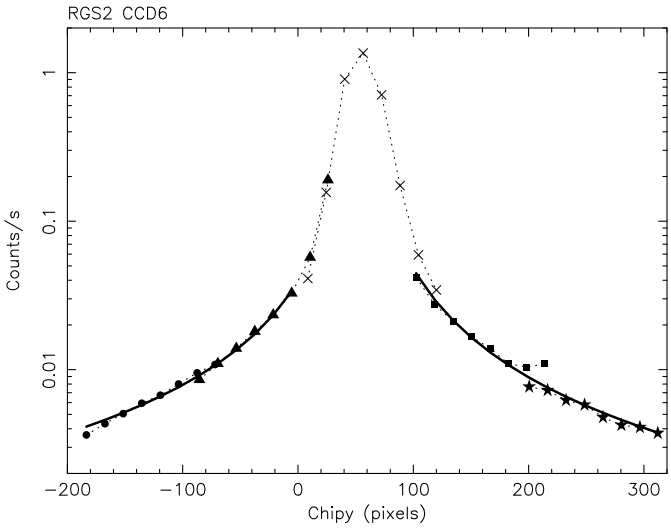

Fig. A.3. Cross dispersion profile for CCD6 of RGS2 for our 5 observations (central and two off-axis pointings at each side). The data have been integrated over the full CCD in the dispersion direction, and over 8 pixels in the cross-dispersion direction. The best-fit power-law models, fitted individually to *chipy* < 0 and *chipy* > 100, are shown by the thick solid lines. Note that we aligned all off-axis pointings to the on-axis (*chipy*) coordinate in the cross-dispersion direction. The different symbols correspond to the different observations.

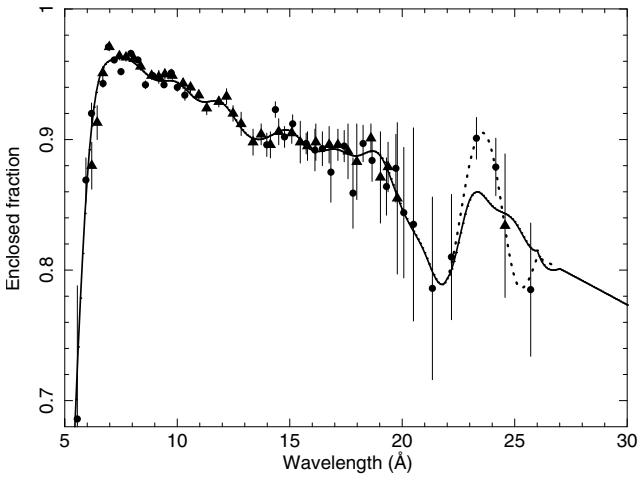

Fig. A.4. Enclosed flux fraction for the on-axis pointing on the Crab as a function of wavelength. Circles are RGS1 data, and triangles RGS2 data, shifted by +0.02 in enclosed fraction. The solid curve shows our finally adopted smoothed approximation to this correction factor; the dotted line shows the original spline fit to the data as described in the text.

First, for RGS2 f_d is on average 0.02 lower than for RGS1, caused by stronger scattering in RGS2. For this reason we have shifted in Fig. A.4 the RGS2 data points by +0.02, in order to eliminate in first order the differences between both RGS detectors.

Secondly, the curve shows fine structure near some important edges, such as the O-K edge (23 Å), Fe-L (17 Å) and Mg K (9 Å) edges. This structure is real and is caused by the dust scattering, which is wavelength dependent and shows structure at these edges (see for example Draine 2003; Costantini et al. 2005). Unfortunately we have insufficient statistics to increase

the wavelength resolution of f_d near these edges. It is also hard to model the fine structure theoretically, as it depends on the chemical and size distribution of the dust grains, the spatial distribution of the underlying synchrotron emission, and the complex redistribution of photons in the combined dispersion/cross-dispersion plane of RGS.

Finally, the accuracy of f_d decreases rapidly towards longer wavelengths, and beyond 25 Å it is impossible to determine it at all. This is caused by an accumulation of several effects, namely (1) the decreasing flux of the Crab nebula towards longer wavelengths due to interstellar absorption; (2) the stronger dust scattering at long wavelengths, making our power-law fits to the spatial profile flatter and hence the correction factors higher and more uncertain; and (3) at the low flux levels of the off-axis pointings at long wavelengths, systematic background uncertainties emerge.

We approximate the data shown in Fig. A.4 as follows. As a first approximation, we fit a power-law to the scattered flux fraction, an assumption that is often made and is based on the Rayleigh-Gans approximation but which however may not be fully appropriate at the longest wavelengths (see for example Smith & Dwek 1998). The power-law is given by $f_d = 1 - 0.00338\lambda^{1.2365}$ with λ the wavelength in Å. A part of this tail is still visible in our model beyond 27 Å, and lacking other data, we use this approximation for all $\lambda > 27$ Å. For the remaining part, we fitted a spline to the residuals of the power-law fit, and added that spline to our correction factor. Around 23 and 24 Å, this spline shows a strong wiggle caused by the two RGS1 data points at those wavelengths (see the dotted curve in Fig. A.4). Such a wiggle is physically not expected and it is perhaps due to a little overshooting of our fit near the end points. It also appears that after spectral fitting the predicted flux in the 1−2 Å wide band just longwards of the O-K edge was too high by up to 4%. Therefore we have fitted a spline to the spectral fit residuals of our preliminary fit in the 23−26 Å range, and included that spline in our final approximation for f_d, the solid curve of Fig. A.4. As our spectral fits show (see Sect. 3.3) this gives reasonable results.

A.7. Broadening in the dispersion direction

The Crab nebula is an extended source. The first order spectrum of any part of the remnant, at projected distance $\Delta\theta$ (in arcmin) along the RGS dispersion axis, will be shifted in wavelength by $\Delta\lambda$ (Å) = $0.138\Delta\theta$. This holds for all wavelengths. Therefore, the intensity profile $I(\theta)$ of Crab, integrated over the cross-dispersion direction for the region covered by the RGS detector, translates directly into a wavelength broadening profile with the same shape. In our spectral fitting, after deriving the source spectrum $S(\lambda)$ we convolve this with the broadening kernel $I(\Delta\lambda)$ before folding with the response matrix. Technically, this is achieved by using the *lpro* convolution model of the SPEX package, which has been used successfully for observations with RGS of several extended X-ray sources like clusters of galaxies, for example Kaastra et al. (2001).

An underlying assumption of this broadening model is that the spatial profile is independent of wavelength. Our discussion of the Chandra imaging data of M04 (Sect. 2.5.2) shows that this is strictly speaking not true for the power-law continuum. However, for the continuum the effect of the broadening is not important, as it varies on much larger wavelength scales than the broadening kernel, and M04 also showed that there is little spatial variation in the interstellar absorption column. Therefore our approximation can be used safely.

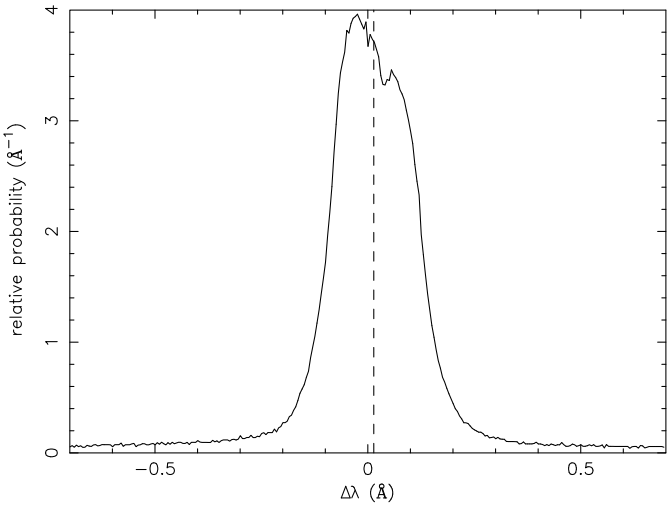

Fig. A.5. Broadening kernel $I(\Delta\lambda)$ to be used to model the spatial extent of Crab in the dispersion direction. The kernel is centred around the nominal position of the pulsar. The average wavelength shift of the kernel is located at $\Delta\lambda = +0.014$ Å and is indicated with the dashed line.

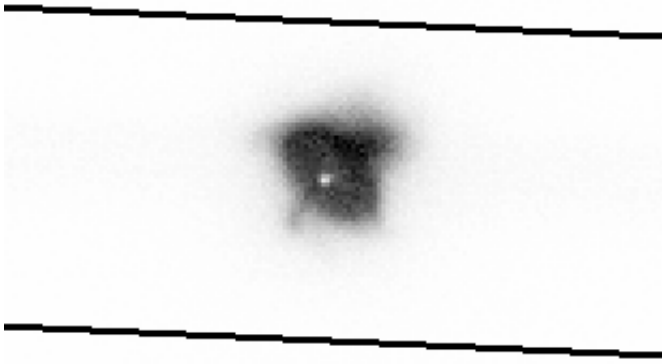

Fig. A.6. MOS1 image of Crab. Shown is a part of the central CCD image of observation 0153750501, on a linear intensity scale. North is up. RGS spectra are extracted between the two parallel lines (separated by 5 arcmin). The pointing is centred on the pulsar, which shows pile-up in this image.

We have constructed the broadening kernel $I(\Delta\lambda)$ using an XMM-Newton observation taken in March 2002 (orbit 411, obsid 0153750501). That observation had the same pointing centre and roll angle as our present observation. MOS1 observed the source in full window mode. The central CCD of MOS1 suffered from severe loss of events due to telemetry limitations, which are more important than pile-up for this source. These telemetry losses do not affect the spectral shape. The remaining fraction of events for the central MOS CCD (3.64%) could be estimated by constructing the projected intensity profiles along each axis and matching that to the projected profiles of the outer CCDs, that do not suffer from telemetry saturation or pile-up. Only the pulsar region suffers from severe pile-up (Fig. A.6), but in the RGS band the pulsar contribution is modest (typically 3−5%). This MOS1 image in the RGS band (0.35−2 keV) was then integrated over the cross-dispersion of RGS, yielding our kernel $I(\Delta\lambda)$. The kernel is shown in Fig. A.5.

The full-width at half maximum of the kernel is 0.22 Å, which therefore is our effective spectral resolution. Our spectra were extracted with respect to the position of the pulsar. The

nebula shows a small asymmetry with respect to that position: the average centre of Crab is shifted by 0.014 Å.

A.8. Spectra used for the spectral fitting

Finally we need to decide which data sets to use. We have spectra in 1, 2, 4 and 8 CCD readout mode. The pile-up corrections increase with the number of CCDs that are readout simultaneously. As a result, the fits for 8 CCD mode may have slightly higher systematic uncertainties than the other spectra. Moreover, the exposure times differ for the readout modes. We have made fits for all combinations 1, 1+2, 1+2+4 and 1+2+4+8 CCD readout mode. As a typical example, the best values for the hydrogen column in units of 10^{25} m^{-2} are 3.174 ± 0.036, 3.175 ± 0.022, 3.184 ± 0.020, and 3.160 ± 0.020 respectively (for model A, without dust). Including the 4 CCD mode data does not improve the statistics significantly, while including the 8 CCD mode data puts the best fit parameter near its 1σ limit, indicating that the value for this mode alone deviates more. For these reasons, we here consider only the combined dataset of single and double CCD readout.

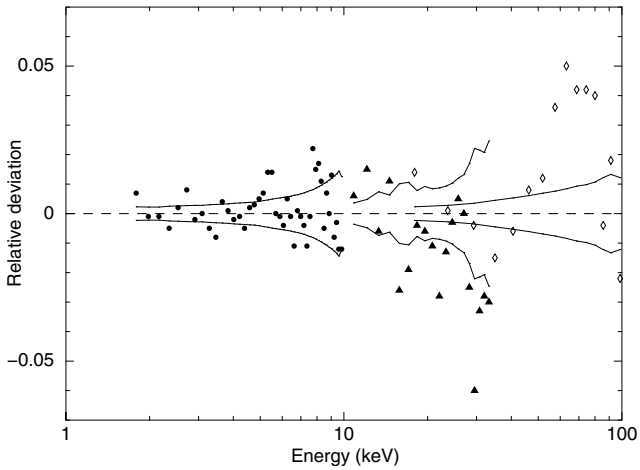

Fig. B.1. Relative residuals of the BeppoSAX measurements of the Crab nebula used by Kuiper et al. (2001) (Fig. 2) compared to the best fit model ($\Gamma = 2.147 \pm 0.002$ and $N = 9.31 \pm 0.05$). For clarity, error bars have been omitted, but the solid lines indicate the $\pm 1\sigma$ *statistical* error range. Circles: MECS; triangles: HPGSPC; diamonds: PDS.

Appendix B: Breakdown of systematic uncertainties

In this Appendix we discuss in more detail the various systematic uncertainties on our derived effective area solution.

B.1. Systematic uncertainties on the adopted spectrum of Crab

B.1.1. Systematic uncertainties on the absolute flux level of Crab

We adopt here the typical uncertainty on the K01 continuum level of 10%. In addition, there is a small uncertainty related to the statistical error of the slope in the K01 data (Sect. 2). However, there are also systematic uncertainties in the shape of the K01 continuum. These are discussed in more detail in the next subsection. We list these uncertainties as column (a) in Table 5.

B.1.2. Systematic uncertainties on the shape of the Crab spectrum

The K01 model that we use for the high energy spectrum of Crab is based on BeppoSAX data. The statistical uncertainties can be determined well (Sect. 2), but it is harder to determine the systematic uncertainties.

For the RGS band, the MECS data are most important so we consider those first. Boella et al. (1997) describe in detail the calibration of the MECS, based on ground measurements and careful modelling of the components of the instrument. Unfortunately, no estimates of systematic uncertainties are given. However, the BeppoSAX cookbook (Fiore et al. 1999) gives some clues.

First, when the total (nebula plus pulsar) Crab data for MECS, HPGSPC and PDS are fitted individually, the photon indices derived from the individual instruments agree to within ±0.016.

Secondly, the BeppoSAX cookbook indicates that the average and dispersion of the PDS to MECS normalisation factor for five different sources excluding Crab, is 0.86 and 0.03, respectively (compare to the value of 0.87 obtained by K01 for Crab). Adopting this scatter of 0.03 as a typical slope uncertainty over the effective centres of the MECS and PDS bands at 4.5 and 45 keV, respectively, we find a corresponding maximum systematic photon index uncertainty of 0.015.

Third, we show in Fig. B.1 in more detail the residuals of the fit presented in Fig. 2. These residuals, corresponding to calibration uncertainties within the instruments, are typically lower than 5% and therefore contribute to systematic uncertainties on the photon index over the 2−100 keV band of at most ±0.012 (=log 1.05/ log 50).

Finally, the latest calibration of INTEGRAL, covering also a broad energy range just like the BeppoSAX data used by K01, gives similar results for the hard X-ray part of the spectrum (Jourdain et al. 2008). Down from 3 keV up to the spectral break at 100 keV, they fit a single power-law with $\Gamma = 2.105 \pm 0.030$ to the full Crab (nebula plus pulsar) spectrum, using exactly the same Galactic foreground absorption model as K01. Over the 2−8 keV band, the K01 model (curved pulsar plus nebula spectrum) has an effective photon index of 2.109, only 0.004 higher than the INTEGRAL value. Moreover, the INTEGRAL flux in this 2−8 keV band is 6% higher than the K01 flux in the same band, well within the quoted 10% uncertainty. Thus, if we would have adopted the INTEGRAL model spectrum instead, the main change would be an overall ∼6% higher flux hence a ∼6% lower effective area for RGS, but no significant slope difference.

The above estimates can be summarised in a maximum systematic slope uncertainty of about 0.016.

B.2. Systematic uncertainties on the curvature correction

The curvature correction based on Chandra imaging of the nebula as derived in Sect. 2.5 has its limitations, leading to systematic uncertainties in its size. We assess these uncertainties here.

B.2.1. Energy range normalisation Chandra continuum

The choice of the 2–8 keV band to normalise the continuum affects the correction slightly. Changing the lower limit by 50% to 1.5 or 3.0 keV modifies $f_c(E)$ typically by less than 2.6%. We list this as column (b) in Table 5.

B.2.2. Local high-energy cut-offs

Some of the local power-law fits of M04 may be affected by unnoted high-energy cut-offs. If this happens, a power-law fit gives a too soft spectrum, resulting in an over-estimate of $f_c(E)$ at low energies. This effect is hard to quantify, but the fact that the photon index of $\Gamma = 2.10$ derived from a direct fit to the total ACIS-S spectrum (M04) agrees well with the spatially integrated spectrum indicates that it is not important. Also, if a significant fraction of the pixels would have a high-energy cut-off, a clear break in the BeppoSAX data used by K01 should be present, which is not the case. The maximum change in photon index for an assumed spectral break near 4 keV in these BeppoSAX data is less than 0.006. This corresponds to a maximum error in f_c of at most 1.4% (column (c)).

B.2.3. Pile-up corrections Chandra

M04 needed to make pile-up corrections; they estimate a systematic uncertainty of 0.05 in their photon indices. As spectral curvature corresponds to differential photon index, the effect is small (less than 0.03%) and we shall ignore it here. Another potential effect might be a systematic error in the pile-up correction of M04 that would correlate with intensity and photon index. The pile-up correction for the photon index Γ of M04 is always less than 0.17 for $\Gamma = 1.5$ and less than 0.21 for $\Gamma = 2.5$. We may assume very conservatively that the maximum systematic error is half of this difference, i.e. 0.02. If we increase and stretch all local photon indices Γ with $\Delta\Gamma(\Gamma) = 0.02(\Gamma - 2.1)$ and re-evaluate the curvature correction, we find differences lower than 0.6% for $\lambda < 30$ Å. As for most wavelength the correction is much lower and the maximum of 0.02 is likely an over-estimate, we can safely ignore this effect here.

B.2.4. Different continuum model for different instruments

In the 1–8 keV band, there is a difference of up to 10% between the model flux of K01 and M04, and a corresponding difference in photon index of 2.147−2.10 = 0.047. Such differences are typical for spectra taken by different instruments, and generally they correspond to calibration uncertainties. As above, we do not expect this difference to produce artificial spectral curvature.

B.2.5. Interstellar absorption column density

There is a big difference between the interstellar absorption N_H used in both papers: K01 have $N_H = 3.61 \times 10^{25}$ m^{-2}, while M04 find 3.20×10^{25} m^{-2}. In the *absorbed* model continuum near the interstellar oxygen edge at 0.53 keV, this causes a 30/50% higher flux below/above the edge in the M04 model as compared to the K01 model. Apparently, the difference is caused by a mismatch of the same order of magnitude between the effective areas of BeppoSAX/LECS and Chandra/ACIS-S near the oxygen edge. Nevertheless, this does not affect the high-energy continuum, and it is also not too important for the determination of the spectral curvature, as that is caused by true spatial variations of the photon index.

B.2.6. Biased absorption due to region selection

The value of N_H derived by M04 may be slightly biased, because in order to avoid pile-up, it was determined in the low surface brightness regions. These regions are mostly found in the outer parts and have softer intrinsic spectra. More importantly, the softest X-ray flux in these regions may be enhanced by up to ∼10% due to dust scattering from the brighter central parts. This may cause a slight under-estimate of the derived interstellar column, as dust scattering is ignored. On the other hand, the same regions may loose soft X-ray flux to regions even further out, thereby reducing the effect. It is therefore hard to quantify this effect, and we will ignore it.

B.2.7. Spatial variations of N_H

M04 assumed that all parts of the nebula have the same interstellar column density. This is a reasonable assumption, as they show that less than 0.5% of all pixels has excess absorption up to 7.5×10^{24} m^{-2} above the average value. The excess is caused by filaments visible in optical line emission. The effect of this on the integrated spectrum is less than 0.3% near the oxygen edge. We list this as column (d) in Table 5.

M04 also estimate that the scatter in N_H due to spatial variations of the interstellar column density is less than 2×10^{24} m^{-2}. For the integrated nebular spectrum, most of these variations will average out; ignoring systematic effects, the uncertainty in the mean absorption for the 2074 pixels considered by M04 would be $\sim \sqrt{2074}$ lower than the scatter, hence about 4×10^{22} m^{-2}, which is undetectable.

B.3. Systematic uncertainties in the absorption model

B.3.1. The role of dust

There are small differences between the continuum model derived from model A (without dust) and model B (with dust). In principle, model B is our preferred model but it still may have its systematic uncertainties, related to issues as the exact density, grain chemical composition and size distribution. As Seward et al. (2006) typically found differences up to 30% in the amount of dust towards Crab depending on their adopted dust model, we will, quite arbitrarily, take here half of the difference between model A and B as the systematic uncertainty associated to the dust model. This is listed in column (f) of Table 5.

B.3.2. Hot gas

The maximum amount of hot gas in the line of sight towards Crab is $N_H \lesssim 5 \times 10^{23}$ m^{-2} (Sect. 4.3.1). We take the transmission of gas with such a column density, proto-solar abundances and a temperature of 0.2 keV as our estimate for the associated systematic uncertainty introduced by ignoring this component (column (g) of Table 5).

B.3.3. The carbon abundance

We follow here Sect. 4.4.1 and adopt a 30% systematic uncertainty in the interstellar carbon abundance. See further column (h) of Table 5.

B.4. systematic uncertainties related to the instrument

B.4.1. The cross-dispersion correction

Our estimate is based on the residuals shown in Fig. A.4 and is shown in column (i) of Table 5.

B.4.2. Pile-up correction

Our estimate is based on Fig. A.2, adopting a 5% (2σ) uncertainty in the pile-up scale parameter a. The uncertainties are shown in Table 5, column (j).

B.4.3. Redistribution errors

We have calibrated the effective area by multiplying the nominal effective area by an empirical fudge factor. However, at short wavelengths important uncertainty is introduced by wide angle scattering of photons by the gratings of RGS. This cannot be described by a simple arf-correction, as it depends on the spectral shape of the source. An estimate of the corresponding uncertainty in the effective area is obtained by comparing the fit residuals for RGS1 and RGS2 separately. We take the difference in residuals, averaged over 1 Å wide bins, as an estimate for the systematic uncertainty associated to this effect. The uncertainties are shown in Table 5, column (k).

B.4.4. Errors in the Chebychev polynomial corrections

Our initial effective area was based on observed spectra of Mrk 421; mismatches between the observed spectra and the adopted power-law continuum of these sources were corrected using a Chebychev polynomial expansion of a correction factor for the effective area of RGS (see Sect. A.2). We estimate the uncertainty associated to this by analysing the fit residuals of another source, PKS 2155-304, orbit 362. The resulting uncertainties are shown in column (l) of Table 5.

B.4.5. Errors in adopted spatial profile in the dispersion direction

The Crab spectrum is energy dependent. We have used a MOS1 image in the 0.35−2.0 keV range to predict the spatial distribution of the emission in the dispersion direction of RGS. We have chosen a number of narrow band energy intervals in the MOS image to see how much that projected profile deviates from the mean 0.35−2.0 keV profile. These intervals range from 8 to 22 Å. We find shifts lower than 1 mÅ in the centroid (to be compared to the *FWHM* of the kernel of 220 mÅ), and no deviations higher than 2% in the *FWHM* of the profile. This justifies our choice of a single broadening kernel.

References

Antia, H. M., & Basu, S. 2005, ApJ, 620, L129
Behar, E., Sako, M., & Kahn, S. M. 2001, ApJ, 563, 497
Boella, G., Chiappetti, L., Conti, G., et al. 1997, A&AS, 122, 327
Costantini, E., Freyberg, M. J., & Predehl, P. 2005, A&A, 444, 187
Cunha, K., Hubeny, I., & Lanz, T. 2006, ApJ, 647, L143
Dame, T. M., Hartmann, D., & Thaddeus, P. 2001, ApJ, 547, 792
de Vries, C. P., Raassen, A. J. J., & Kaastra, J. S. 2008, in preparation
Del Zanna, L., Volpi, D., Amato, E., & Bucciantini, N. 2006, A&A, 453, 621
den Herder, J. W., Brinkman, A. C., Kahn, S. M., et al. 2001, A&A, 365, L7
Draine, B. T. 2003, ApJ, 598, 1026
Drake, J. J., & Testa, P. 2005, Nature, 436, 525
Esteban, C., Peimbert, M., García-Rojas, J., et al. 2004, MNRAS, 355, 229
Ferrière, K. M. 2001, Rev. Mod. Phys., 73, 1031
Fiore, F., Guainazzi, M., & Grandi, P. 1999, Cookbook for BeppoSAX NFI Spectral Analysis, availabe at http://heasarc.gsfc.nasa.gov/docs/sax/abc/saxabc/saxabc.html
Isaacman, R., & Rankin, J. M. 1977, ApJ, 214, 214
Jourdain, E., Götz, D., Westergaard, N. J., Natalucci, L., & Roques, J. P. 2008, Proc. of Science, in press [arXiv:0810.0646]
Juett, A. M., Schulz, N. S., & Chakrabarty, D. 2004, ApJ, 612, 308
Juett, A. M., Schulz, N. S., Chakrabarty, D., & Gorczyca, T. W. 2006, ApJ, 648, 1066
Kaastra, J. S., Mewe, R., & Nieuwenhuijzen, H. 1996, in UV and X-ray Spectroscopy of Astrophysical and Laboratory Plasmas, ed. K. Yamashita, & T. Watanabe, 411
Kaastra, J. S., Ferrigno, C., Tamura, T., et al. 2001, A&A, 365, L99
Kaastra, J. S., Steenbrugge, K. C., Raassen, A. J. J., et al. 2002, A&A, 386, 427
Kaastra, J. S., de Vries, C. P., den Herder, J. W. A., et al. 2009a, A&A, in preparation (Paper III)
Kaastra, J. S., Lanz, T., Hubeny, I., & Paerels, F. B. S. 2009b, A&A, 497, 311 (Paper II)
Kirsch, M. G., Briel, U. G., Burrows, D., et al. 2005, Proc. SPIE, 5898, 22
Kuiper, L., Hermsen, W., Cusumano, G., et al. 2001, A&A, 378, 918
Ling, J. C., & Wheaton, W. A. 2003, ApJ, 598, 334
Lodders, K. 2003, ApJ, 591, 1220
Lundgren, S. C., Cordes, J. M., Ulmer, M., et al. 1995, ApJ, 453, 433
Mori, K., Burrows, D. N., Hester, J. J., et al. 2004, ApJ, 609, 186
Morrison, R., & McCammon, D. 1983, ApJ, 270, 119
Paerels, F., Brinkman, A. C., van der Meer, R. L. J., et al. 2001, ApJ, 546, 338
Predehl, P., & Klose, S. 1996, A&A, 306, 283
Predehl, P., & Schmitt, J. H. M. M. 1995, A&A, 293, 889
Sako, M., Kahn, S. M., Behar, E., et al. 2001, A&A, 365, L168
Savage, B. D., Bohlin, R. C., Drake, J. F., & Budich, W. 1977, ApJ, 216, 291
Schattenburg, M. L., & Canizares, C. R. 1986, ApJ, 301, 759
Seward, F. D., Gorenstein, P., & Smith, R. K. 2006, ApJ, 636, 873
Smith, R. K., & Dwek, E. 1998, ApJ, 503, 831
Sollerman, J., Lundqvist, P., Lindler, D., et al. 2000, ApJ, 537, 861
Temim, T., Gehrz, R. D., Woodward, C. E., et al. 2006, AJ, 132, 1610
Tennant, A. F., Becker, W., Juda, M., et al. 2001, ApJ, 554, L173
Toor, A., & Seward, F. D. 1974, AJ, 79, 995
van Aken, P. A., Liebscher, B., & Styrsa, V. J. 1998, Phys. Chem. Miner., 25, 494
van Aken, P. A., & Liebscher, B. 2002, Phys. Chem. Miner., 29, 188
Verner, D. A., & Yakovlev, D. G. 1995, A&AS, 109, 125
Weisskopf, M. C., Hester, J. J., Tennant, A. F., et al. 2000, ApJ, 536, L81
Weisskopf, M. C., O'Dell, S. L., Paerels, F., et al. 2004, ApJ, 601, 1050
Willingale, R., Aschenbach, B., Griffiths, R. G., et al. 2001, A&A, 365, L212
Wilms, J., Allen, A., & McCray, R. 2000, ApJ, 542, 914
Yao, Y., & Wang, Q. D. 2006, ApJ, 641, 930